Eduardo Balbinot

Aglomerados de estrelas em estado avançado de dissolução: estudos de caso no Grupo Local.

Porto Alegre

2011

Eduardo Balbinot

Aglomerados de estrelas em estado avançado de dissolução: estudos de caso no Grupo Local.

Dissertação realizada sob orientação do Professor Dr. Basílio Xavier Santiago e apresentada ao Programa de pós-graduação em Física da UFRGS em preenchimento parcial dos requisitos para a obtenção do título de Mestre em Física.

INSTITUTO DE FÍSICA
UNIVERSIDADE FEDERAL DO RIO GRANDE DO SUL

Porto Alegre

2011

Astronomy is useful because it raises us above ourselves; it is useful because it is grand; that is what we should say. It shows us how small is man's body, how great his mind, since his intelligence can embrace the whole of this dazzling immensity, where his body is only an obscure point, and enjoy its silent harmony. Thus we attain the consciousness of our power, and this is something which can not cost too dear, since this consciousness makes us mightier.

[Henri Poincaré (1854 - 1912†) - *The Value of Science* 1904]

Sumário

Resumo

Neste trabalho é apresentado o estudo de aglomerados de estrelas em três ambientes distintos. Os efeitos do ambiente são discutidos do ponto de vista observacional tendo como objetivo principal buscar fenômenos tipicamente associados às condições dinâmicas, às quais cada aglomerado está submetido.

Os ambientes estudados são:

i. O bojo da Via Láctea, dominado por fortes interações gravitacionais devido à grande concentração de matéria. Nesse ambiente espera-se que exista um alto grau de evaporação estelar nos aglomerados. O aglomerado NGC 6642 encontra-se diretamente sobre o bojo e é estudado em busca de efeitos previstos para esse ambiente. Encontramos que uma combinação de segregação de massa e forte evaporação estelar levou à inversão da função de massa desse aglomerado, de modo que possui mais estrelas massivas do que menos massivas.

ii. A Grande Nuvem de Magalhães, que possui uma lacuna na distribuição de idade de seus aglomerados. Esse fenômeno tem origem possivelmente na interação com sua companheira, a Pequena Nuvem de Magalhães. Durante a interação mais intensa, a formação estelar e consequentemente de aglomerados foi alterada. Diversos aglomerados da Grande Nuvem de Magalhães tiveram determinações de idade consistentes com a lacuna de idades, porém utilizando magnitudes e cores integradas, um método menos preciso. Neste trabalho buscamos estudar em detalhe a população estelar resolvida destes candidatos à lacuna de idades e de fato classificados como um dos raros integrantes da lacuna. Constatamos, no entanto, que nenhum dos candidatos estudados de fato possui idade consistente com a lacuna de idades.

iii. O halo externo da Galáxia. Neste ambiente a interação de maré é menos intensa que no bojo. No entanto a interação com o disco é significativa quando a órbita do aglomerado intersecta o plano do disco. Os aglomerados Palomar 5 e NGC 2298 são exemplos de aglomerados que possuem órbitas desse tipo. Palomar 5 possui extensas caudas de maré oriundas da evaporação de estrelas, porém NGC 2298 não possui nenhuma detecção conclusiva de caudas ou estruturas de maré. Neste trabalho testamos uma implementação do método de *matched-filter* para detecção de caudas de maré. Esse método é testado no aglomerado Palomar 5, utilizando dados do SDSS, onde detectamos com sucesso as caudas de maré deste aglomerado. O método também é amplamente testado em simulações de aglomerados com caudas de maré. Finalmente aplicamos o *matched-filter* ao caso de NGC 2298. Diversas estruturas de maré são encontradas com nível de confiabilidade acima de 1σ, no entanto as estruturas encontradas são menos coerentes que as caudas de maré de Palomar 5.

1 Introdução

Aglomerados de estrelas estão entre os objetos mais antigos no Universo. Suas idades variam de alguns milhões até cerca de 14 bilhões de anos, sendo assim testemunhas dos processos primordiais de formação das galáxias e, por consequência, do Universo como um todo.

Dentro do paradigma de formação de estruturas no modelo cosmológico ΛCDM, onde estruturas menores dão origem a estruturas maiores através de fusões, os aglomerados podem ser vistos como os blocos construtores mais fundamentais. Dentro desse cenário hierárquico entender como os aglomerados entregam seu conteúdo estelar para as galáxias hospedeiras é entender uma parte fundamental do processo de formação das galáxias.

Os aglomerados de estrelas são historicamente divididos em duas classes: os aglomerados abertos e os aglomerados globulares. Os aglomerados abertos são caracterizados pelo menor número de estrelas ($10^2 - 10^4$), pela forma irregular e uma idade menor que ~ 1 Gyr, enquanto os aglomerados globulares podem conter até $\sim 10^6$ estrelas, possuindo uma forma esferoidal e idades ultrapassando os 10Gyr.

Com a evolução das técnicas de observação astronômica o censo de aglomerados globulares em nossa Galáxia está perto da completude. A aparente dicotomia entre aglomerados abertos e globulares se tornou incerta devido a observação de objetos cujas características invadem a definição de cada uma das classes. Por exemplo, o aglomerado aberto Berkeley 17 tem uma idade de 10 Gyr (Salaris et al., 2004) - uma idade antes típica apenas de aglomerados globulares, porém ainda com uma forma irregular.

De maneira semelhante, o censo de aglomerados abertos progrediu a passos largos com o advento de levantamentos fotométricos no infravermelho - faixa de comprimentos de onda que evita absorção pela poeira do disco da Galáxia. Um desses levantamentos é o 2MASS que elevou o número de aglomerados abertos conhecidos para a casa dos milhares. Por serem jovens, os aglomerados abertos traçam a formação estelar recente em uma galáxia, tornando-se importantes ferramentas para mapear a estrutura de braços espirais no disco [e.g. Bica et al. (2006)].

O censo de aglomerados progrediu não só na Via Láctea, mas também em galáxias do Grupo Local, em especial nas Nuvens de Magalhães. Tanto a Grande quanto a Pequena Nuvem de Magalhães (LMC e SMC respectivamente), possuem aglomerados globulares jovens que são os análogos dos aglomerados globulares, muito mais velhos, que vemos hoje na Galáxia. A existência desses objetos em uma galáxia próxima possibilita o confronto dos modelos de evolução estelar com uma classe de aglomerados não existente na Via Láctea.

Uma das mais marcantes características do sistema de aglomerados da LMC é a presença de uma lacuna de idades. Ou seja, existe um domínio de idades, entre 4 e 10 Gyr, onde praticamente não existem aglomerados. A origem da lacuna ainda é incerta, porém certamente está associada a um período onde a taxa de formação de estrelas ou a taxa de formação de aglomerados foi alterada. Como a LMC interage periodicamente com sua companheira, a SMC, e ambas interagem com a Galáxia, podemos supor que alterações bruscas na formação de aglomerados têm ligação com estes eventos de interação.

O estudo de sistemas de aglomerados em outras galáxias revelou uma barreira ainda mais difusa na classificação de aglomerados de estrelas. A descoberta dos *Diffuse Star Cluster* (DSC) e dos *Faint Fuzzies* (FF), que possuem magnitude consistentes com aglomerados globulares típicos, porém possuem um brilho superficial muito baixo, ou seja, são maiores que um globular típico (Peng et al., 2006; Larsen et al., 2000). Essas novas classes de aglomerados começam a ter propriedades similares a algumas galáxias anãs.

Apesar de possuir algumas lacunas, existe uma relação clara entre sistemas estelares - especialmente os mais velhos - que os une através de propriedades dinâmicas comuns. Forbes et al. (2008) fez um levantamento extenso sobre as propriedades de sistemas estelares velhos, mostrando que existe uma conexão entre aglomerados globulares e galáxias elípticas. Esta relação abrange não somente estas duas classes de objetos mas também as galáxias anãs supercompactas e objetos de transição de massa intermediária [Geha et al. (2003) e referências]. Essa semelhança do ponto de vista dinâmico mostra a existência de uma similaridade entre o grande e o pequeno nos sistemas estelares no Universo, algo previsto nos modelos cosmológicos ΛCDM.

A similaridade entre as estruturas em grande e pequena escala reflete uma origem única para estes sistemas estelares. Muito mais do que uma origem única, estes objetos compartilham propriedades dinâmicas similares. Contudo, a grande diferença entre sistemas estelares menores e maiores é a presença de matéria escura. As galáxias anãs esferoidais são dominadas por matéria escura e portanto suas estrelas têm uma dispersão de velocidades maior. Por outro lado, os aglomerados globulares, muito menos massivos que as galáxias anãs, não possuem nenhuma evidência de possuir halos de matéria escura. Vê-se que a diferença fundamental entre a origem

destes dois sistemas estelares está diretamente ligada a presença ou não de matéria escura.

Apesar dos esforços recentes [Gilmore et al. (2007) e referências] ainda há grande incerteza na quantidade de matéria escura em galáxias anãs esferoidais. Objetos de transição entre aglomerados globulares e galáxias possuem ainda maior incerteza em suas propriedades, uma vez que não há contrapartida observada destes objetos no Grupo Local. Resta-nos buscar por estes objetos e compreender o papel da matéria escura na origem e evolução destes sistemas esferoidais sustentados por pressão dinâmica.

1.1 Efeitos dinâmicos

Ainda como consequência da formação hierárquica, a população de aglomerados que vemos hoje em qualquer galáxia é apenas uma fração daquela que foi um dia. Por exemplo, assim que as primeiras estrelas de um aglomerado se formam, ventos estelares ejetam o gás remanescente mudando abruptamente o potencial gravitacional do sistema. Essa mudança brusca pode levar à completa dissolução do aglomerado em uma escala de tempo de milhões de anos. Esse fenômeno, chamado mortalidade infantil, foi observado pela primeira vez em nossa Galáxia por Lada & Lada (2003) ao comparar o número de aglomerados abertos embebidos em gás com aqueles livres de gás.

Uma gama de outros fenômenos colaboram para a destruição dos aglomerados. Sua dinâmica interna, governada pela relaxação de dois corpos, faz com que as estrelas sejam gradualmente ejetadas. Esse processo lento de ejeção pode levar centenas de tempos de relaxação (Binney & Tremaine, 1987). No entanto, a influência externa pode acelerar o processo de dissolução de um aglomerado. Spitzer & Thuan (1972) mostrou que a presença de um campo de maré acelera o processo de dissolução consideravelmente. Quando comparado com um aglomerado isolado, o aglomerado imerso em um campo de maré perde até 4 vezes mais estrelas, podendo perder até metade de suas estrelas antes do colapso do núcleo (ver §2).

Outra clara evidência de influência externa sobre um aglomerado é a existência de um raio de maré. Ele é definido como sendo a distância ao centro do aglomerado na qual a influência gravitacional da galáxia é igual a do aglomerado. Nesse sentido o raio de maré marca a região além da qual as estrelas se tornam desligadas do aglomerado. A existência de um raio de maré, ou raio limite, é claramente visível nas observações dos aglomerados de nossa Galáxia (Trager et al., 1995; King, 1962).

Enquanto um aglomerado orbita o centro da Galáxia ele experimenta um campo gravitacional que varia lentamente, o que causa pouco ou nenhum efeito sobre sua estrutura, além da

existência de um raio limite (citado acima). No entanto, quando a órbita do aglomerado cruza o disco ou o bojo da Galáxia uma mudança brusca no potencial é feita, diminuindo assim o raio de maré em uma escala de tempo menor que o tempo dinâmico do aglomerado. Essa mudança no potencial faz com que estrelas outrora ligadas sejam desligadas do aglomerado, criando um caminho preferencial para a fuga de estrelas ao longo da linha de ação do campo de maré. Uma estrela que se desliga do aglomerado pela parte externa de sua órbita é deixada para trás enquanto estrelas que são desligadas pela parte interna ficam adiantadas na órbita. Portanto, um aglomerado deixa uma trilha de estrelas que traça aproximadamente a sua órbita, pois a dispersão de velocidades das estrelas em um aglomerado é muito menor que a velocidade orbital do aglomerado (ver §4). Esta trilha de estrelas pode ser usada para melhor entender o potencial da Galáxia (Koposov et al., 2010).

Baumgardt et al. (2003) mostraram, utilizando simulações N-Corpos, que a fuga de estrelas de um aglomerado que sofre sucessivas passagens pelo disco/bojo se dá preferencialmente para estrelas de baixa massa. Isso é devido ao processo de segregação de massa, onde estrelas menos massivas migram para a periferia do aglomerado, enquanto as mais massivas migram para as regiões centrais. Portanto, estrelas mais próximas do raio de maré possuem massas menores e são preferencialmente depletadas. Esse fenômeno foi observado em diversos aglomerados, sugerindo um alto grau de dependência do ambiente sobre o conteúdo estelar destes objetos (Andreuzzi et al., 2001; de Marchi et al., 2007; Balbinot et al., 2009).

Vemos portanto as inúmeras facetas dos processos envolvidos na destruição de aglomerados, sendo a maneira com que um sistema de aglomerados evolui para chegar ao seu estado atual extremamente complexa e ainda não completamente compreendida. A evolução destes sistemas depende fortemente de como cada aglomerado se dissolve e entrega seu conteúdo estelar para a população de campo da galáxia hospedeira. Nesse sentido devemos buscar compreender todos efeitos dinâmicos que podem acelerar ou desacelerar a taxa de destruição de aglomerados, bem como sua dependência com o ambiente onde estes objetos se encontram. Para obter tal grau de conhecimento sobre estes objetos necessitamos acesso a sua população estelar resolvida. Com a tecnologia atual conseguimos este feito apenas para estrelas dentro de nossa Galáxia e nas galáxias mais próximas, nossas vizinhas dentro do Grupo Local.

1.2 Os estudos de caso

Apesar de restrito a uns poucos membros do Grupo Local, conseguimos ter acesso a uma gama de ambientes dinamicamente distintos. Neste trabalho propomos estudar aglomerados

cujas estrelas podem ser espacialmente resolvidas. Para tal empregamos uma variedade de ferramentas de análise do diagrama cor-magnitude (CMD), sempre que possível utilizando a comparação direta com modelos de evolução estelar. Com estes dados procuramos extrair o máximo de informação sobre a dinâmica destes aglomerados de estrelas e como o ambiente onde se encontram influenciou sobre seu estado atual.

Por terem se formado de uma mesma nuvem molecular, as estrelas de um aglomerado possuem aproximadamente a mesma composição química, idade e distância em relação ao observador. Esse tipo de população estelar é denominado população estelar simples (SSP). A teoria de evolução estelar é capaz de prever a posição no CMD das estrelas de uma SSP, ou seja, possibilitando a comparação direta dos modelos evolutivos com os aglomerados de estrelas. Desse ponto de vista os aglomerados de estrelas são laboratórios para teoria de evolução estelar permitindo o confronto dos modelos com dados observacionais como, por exemplo, composição química obtida pela espectroscopia de estrelas individuais.

Nesta dissertação desenvolvemos diversas técnicas de análise de CMDs com intuito de estudar aglomerados de estrelas em ambientes dinamicamente distintos. Utilizando estas técnicas buscamos entender quais os efeitos são mais pronunciados em cada caso, estudando as particularidades de cada aglomerado ou sistema de aglomerados.

O aglomerado NGC 6642 se encontra muito próximo do centro da Galáxia, sugerindo a presença de grandes forças de maré além de choques com o bojo. Estas características fazem deste aglomerado um bom candidato para se buscar a influência de um ambiente dinamicamente violento sobre o seu conteúdo estelar. NGC 6642 também é um aglomerado muito velho e portanto suas estrelas existem a tempo suficiente para que sua dinâmica interna atue de maneira pronunciada, levando ao colapso do núcleo.

Como segundo estudo de caso tomamos aglomerados da LMC candidatos a pertencerem à lacuna de idades. Estes objetos foram primeiramente classificados utilizando-se fotometria integrada e foi constatado que possuem idades dentro do intervalo que vai de 4 a 10 Gyr (Hunter et al., 2003). Nesse estudo buscamos analisar cuidadosamente a população estelar resolvida destes candidatos e de fato classificá-los ou não com idades dentro da lacuna. Os aglomerados estudados possuem baixa massa e, portanto, podem ser os últimos remanescentes de uma população muito mais numerosa de aglomerados formados na LMC durante a época de formação da lacuna de idades.

Finalmente, o último caso estudado é o aglomerado globular do halo NGC 2298. Esse aglomerado possui uma função de massa invertida (de Marchi et al., 2007), evidência de uma influência pronunciada do ambiente. Sua órbita é extremamente rasa, tangente ao disco da

Galáxia - o que pode causar frequentes choques com o disco e influência de maré proveniente da quantidade de matéria no disco. Neste aglomerado buscamos por evidências de ejeção de estrelas e a formação de estruturas (halos ou caudas) além de seu raio de maré.

2 O aglomerado globular do bojo NGC 6642

A população conhecida de aglomerados globulares (GCs) do bojo é composta por aglomerados relativamente ricos em metais com alta razão de elementos alfa (Mg, Ti, Ca, Si, S, Ne, etc) em relação ao Ferro ($[\alpha/Fe]$), o que indica que a formação de estrelas naquela região se deu de maneira rápida durante os primeiras estágios de formação da Galáxia (Origlia et al., 2005). Portanto, o bojo é um local apropriado para buscar GCs velhos com metalicidades distintas daqueles do halo. O bojo é um ambiente denso quando comparado com o halo, logo esperamos que exista uma evolução dinâmica diferenciada para os GCs neste ambiente, pois estes sofrem choques e possuem forças de maré mais pronunciadas devido à proximidade do centro galático (Aguilar et al., 1988).

Por ser um aglomerado antigo, com idade comparável a da Galáxia, esperamos encontrar suas estrelas em um estágio avançado de evolução dinâmica. Como qualquer sistema de partículas interagentes através da força gravitacional, em um dado momento tenderá ao colapso devido a relaxação de dois corpos - fenômeno também conhecido como colapso gravo-térmico ou colapso do núcleo. No processo de colapso a densidade central de estrelas cresce de maneira desenfreada, podendo levar a uma distância típica entre as estrelas igual a distância do Sol até Plutão. Muitos aglomerados globulares de nossa Galáxia já deveriam ter colapsado, no entanto têm seus núcleos inflados até hoje (De Marchi et al., 2007). O efeito do colapso do núcleo é visto em simulações N-Corpos realísticas de aglomerados globulares. Nestas simulações a única maneira de frear o colapso é introduzindo uma fração de 100% de estrelas binárias, ou seja, todas as estrelas do aglomerado simulado possuem uma companheira. As estrelas binárias funcionam como um reservatório de energia durante as interações com uma terceira estrela. Ao interagir com uma terceira estrela o sistema binário doa parte de sua energia potencial para a estrela passageira, que ganha energia cinética. O aumento das velocidades das estrelas no núcleo faz que ele seja inflado, afastando-o do estágio de colapso do núcleo. Diversos estudos foram conduzidos para avaliar os efeitos do binarismo na dinâmica dos aglomerados, entre eles estão os trabalhos de Wilkinson et al. (2003) e Mackey et al. (2008).

Wilkinson et al. (2003) mostrou que ao introduzir uma população de binárias o aglomerado consegue sustentar o núcleo após o colapso, no entanto as escalas de tempo para que o núcleo seja inflado novamente são maiores que o observado. Mackey et al. (2008) introduz não só binárias, mas também buracos negros e remanescentes estelares (anãs brancas e estrelas de nêutrons). Estes novos componentes adicionados ao aglomerado simulado mostram que buracos negros binários são os responsáveis pela maior parte da pressão que sustenta o núcleo após o colapso.

Outro efeito esperado para um aglomerado dinamicamente evoluído, como NGC 6642, é a segregação de massa. Nesse caso, através da equipartição de energia entre as estrelas do aglomerado, aquelas com maior massa tendem a migrar para regiões mais internas, enquanto as menos massivas migram para periferia.

O GC NGC 6642 é um excelente candidato para observar os efeitos dinâmicos citados acima. Este aglomerado está localizado logo acima do bojo da Galáxia em uma região de transição halo-bojo. Tanto pela distância quanto pela alta densidade de NGC 6642 a análise de sua estrutura e evolução dinâmica requer imageamento de alta resolução espacial, para que seja possível separar estrelas individuais mesmo nas regiões mais internas. Isso é possível utilizando a *Advanced Camera for Surveys* no modo *Wide Field Channel* (ACS/WFC) a bordo do *Hubble Space Telescope* (HST).

Neste capítulo será apresentado o artigo publicado oriundo do estudo fotométrico do aglomerado NGC 6642, utilizando dados do HST com a câmera ACS no modo WFC. Os dados utilizados fazem parte do arquivo público do *Space Telescope Science Institute* (STScI) e são parte da proposta 9799, observada em 2004.

Mon. Not. R. Astron. Soc. **396,** 1596–1602 (2009) doi:10.1111/j.1365-2966.2009.14819.x

The globular cluster NGC 6642: evidence for a depleted mass function in a very old cluster

E. Balbinot,⋆ B. X. Santiago, E. Bica and C. Bonatto

Departamento de Astronomia, Universidade Federal do Rio Grande do Sul, Av. Bento Gonçalves 9500, Porto Alegre 91501-970, RS, Brazil

Accepted 2009 March 24. Received 2009 March 23; in original form 2009 January 19

ABSTRACT

We present photometry for the globular cluster NGC 6642 using the F606W and F814W filters with the Advanced Camera for Surveys in the Wide Field Channel (ACS/WFC) third generation camera on board of *Hubble Space Telescope*. The colour–magnitude diagram shows sources reaching ≈6 mag below the turn-off in $m_{\rm F606W}$. A theoretical isochrone fitting was performed and evolutionary parameters were obtained, such as the metallicity [Fe/H] = −1.80 ± 0.2 and age $\log[\tau({\rm yr})] = 10.14 \pm 0.05$. We confirm that NGC 6642 is located in the Galactic bulge, with a distance to the Sun $d_\odot = 8.05 \pm 0.66$ kpc and the reddening $E(B-V) = 0.46 \pm 0.02$. These values are in general agreement with those of previous authors. About 30 blue stragglers were found within the central 1.6 pc of NGC 6642. They are strongly concentrated to the very central regions. The cluster displays a well-developed horizontal branch (HB), with a much redder morphology than that of typical old halo globular clusters of similar metallicity. Completeness-corrected luminosity and mass functions were obtained for different annuli centred on NGC 6642. Their spatial variation indicates the existence of mass segregation and depletion of low-mass stars. Most striking is the inverted shape of the mass function itself, with an increase in number as a function of increasing mass. This has been previously observed in other globular clusters and is also the result of *N*-body simulations of stellar systems which have undergone ≃90 per cent of their lifetime and which are subjected to strong tidal effects. We also analysed the density profile and concluded that NGC 6642 has a collapsed core, provided completeness effects are correctly accounted for. We thus conclude from independent means that NGC 6642 is a very old, highly evolved, core-collapsed globular cluster with an atypical HB morphology. Its current location close to perigalactic, at only 1.4 kpc from the Galactic Centre, may contribute to this high level of dynamical evolution and stellar depletion.

Key words: globular clusters: general – globular cluster: individual: NGC 6642 – Galaxy: structure.

1 INTRODUCTION

Given their relatively high contrast with the background, the census of globular clusters (GCs) in the Galaxy is near completion. The dense and highly extincted Galactic bulge, specially its inner regions, is the site where most missing clusters, perhaps 10 per cent of the total known population, are expected to be (Ivanov, Kurtev & Borissova 2005; Ortolani, Bica & Barbuy 2006 and references therein). The bulge is known to host old but fairly metal-rich stellar populations, with high [α/Fe] ratios, indicating that it formed on a short time-scale early in the Galactic history (Origlia et al. 2005). The bulge is thus an appropriate region to look for ancient GCs with distinct metallicities from those in the outer stellar halo. The bulge environment may also cause extreme dynamical evolution of star clusters due to bulge shocking and strong tidal effects (Aguilar, Hut & Ostriker 1988; Shin, Kim & Takahashi 2008). For old enough GCs, effects of close stellar encounters, which lead to mass segregation and stellar evaporation, are certain to be found in them as well (Baumgardt & Makino 2003).

Analyses of the structure and dynamical evolution of bulge GCs require high-resolution imaging in order to resolve individual stars in their cores and to effectively subtract contaminating field stars. The Advanced Camera for Surveys in the Wide Field Channel (ACS/WFC) on board of the *Hubble Space Telescope* (*HST*) has provided a significant leap in the amount of such data on GCs, not only in the bulge but also elsewhere (Sarajedini et al. 2007; Richer et al. 2008; Paust et al. 2009). Recently, Martin-Franch et al. (2008) provided ACS photometry for 64 halo GCs and derived relative ages. The ACS allows us to study extremely dense fields

⋆E-mail: eduardo.balbinot@ufrgs.br

using point source photometry. With such technique, it is feasible to use stellar interior models to obtain evolutionary parameters of the cluster stellar population.

NGC 6642 (also designated by ESO 522-SC32 and GCl-97) is located at $l = 9.^{\circ}81, b = -6.^{\circ}44$, therefore projected towards the Galactic bulge. It is thus superimposed on to bulge and inner halo stellar populations. Dynamical studies of this GC, as well as other bulge clusters, have thus been extremely difficulty, due to limitations of ground based images. Structural parameters were found by Trager, King Ivan & Djorgovski (1995), such as core radius $r_{\rm core} = 6.1$ arcsec, concentration parameter $c = 1.99$ and half light radius $r_{\rm h} = 44$ arcsec. They also conclude that NGC 6642 is a core-collapsed candidate. Using spectroscopy of individual stars, Minniti (1995) derived [Fe/H] $= -1.40$. Later Barbuy et al. (2006) using *BVI* photometry with Southern Observatory for Astrophysical Research (SOAR) found [Fe/H] $= -1.3$, reddening $E(B-V) = 0.42 \pm 0.03$ and $\mathrm{d}_{\odot} = 7.2$ Kpc [$(m-M)_0 = 14.3$]. In the catalogue compiled by Harris (1996), similar results are quoted: $(m-M)_V = 15.90$, $E(B-V) = 0.41$ and [Fe/H] $= -1.35$. All these results are from ground-based studies. The only space-based data set on NGC 6642 so far is that from the compilation of colour–magnitude diagrams (CMDs) from Piotto et al. (2002), who used the Wide Field Planetary Camera 2 snapshots.

In this work, we present F606W (broad *V*) and F814W (broad *I*) ACS photometry of NGC 6642. Note that NGC 6642 is not included in the sample by Martin-Franch et al. (2008) since it is projected towards the bulge. We use this photometry not only to derive metallicity, reddening, distance and age, but also to make a detailed analysis of its, for example, structure, including radial density profile (RDP), luminosity and mass functions, horizontal branch (HB) morphology and blue stragglers (BSs). This paper is organised in the following way. In Section 2, we describe the data and the reduction process. In Section 3, we present the data analysis. In Section 4, there is a brief discussion on the cluster age and evolution; we also present the concluding remarks.

2 DATA

The images were retrieved from the Space Telescope Science Institute[1] (STScI) data archive and were automatically reduced by the STScI pipeline, i.e. they were corrected for bias, dark current and were divided by the flat-field image. The images of NGC 6642 are part of the proposal 9799 and were obtained in 2004. They cover a $202 \times 202\,\mathrm{arcsec}^2$ field of view at a spatial scale of $0.049\,\mathrm{arcsec\,pixel}^{-1}$, with a gap between the CCDs. Two exposures were taken in the F606W and F814W filters: short (10 s) and long (340 s). In Fig. 1, we show the F814W short exposure for the cluster's central region. Note the detached bright central object composed by unresolved individual stars located near the cluster centre.

The photometry was carried out using the DOLPHOT software (Dolphin et al. 2000). The following steps were taken to prepare the images for photometry: (i) the task ACSMASK masks all bad pixels and (ii) the task SPLITGROUPS splits the multi-extension FITS image into single chip images. As described in the DOLPHOT manual, a position reference image must be adopted, preferentially a deep and uncrowded one. We used the F814W long exposure with geometric corrections applied (drizzled image) as the reference frame. The photometric measurements were performed on the calibrated

[1] http://www.stsci.edu/

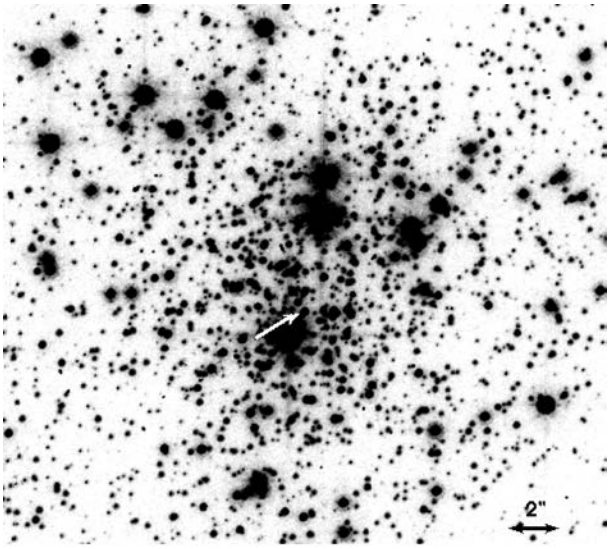

Figure 1. NGC 6642: central region ($22 \times 21\,\mathrm{arcsec}^2$) of the F814W short exposure. north is up and east is right. The adopted centre is indicated by the white arrow. Note the dense object, apparently formed by a clump of crowded stars just below the centre of this image. Even with ACS/*HST* the stars in the centre of NGC 6642 are not easily resolvable.

frames, not corrected for geometric distortions. We adopted the recommended parameters in the DOLPHOT manual. The output magnitudes, in the vegamag system, were corrected for aperture and charge transfer efficiency (CTE). The output position of each star is subsequently corrected for geometrical distortion using the reference frame.

In order to have a high-quality CMD of NGC 6642, the output parameters of DOLPHOT were used to filter out non-stellar objects, cosmic rays and other spurious detections such as wings and diffraction rings. Basically, the *sharpness* parameter measures if the source is too sharp (positive values) or extended (negative values). The *crowding* parameter measures how much the light of a star is due to close neighbours used in the point spread function fit. As recommended in DOLPHOT, no χ^2 cut has been applied as a star selection criterion, due to its dependence on brightness. The following cuts were used: $-0.1 \leq$ sharpness ≤ 0.1; crowding ≤ 0.6; roundness ≤ 0.35. Only stars with type 1 and error type less than 8 in the DOLPHOT classification system were kept. The total number of stars found with accurate photometry in both passbands is $\sim$32 000.

A sanity check was performed to verify the quality of our photometry. We applied the bandpass transformation given by Sirianni et al. (2005) to convert the observed HB and main-sequence turn-off (MSTO) magnitudes and colours from F606W and F814W to Johnson *V* and *I*. They were then compared to the CMD from Barbuy et al. (2006). We have $V_{\rm HB} = 16.40 \pm 0.03$ as the mean HB *V*-band magnitude and associated error, whereas Barbuy et al. (2006) got $V_{\rm HB} = 16.35 \pm 0.04$. As for the MSTO, our CMD yields $(V, V-I) = (19.75, 0.94)$, compared to $(V, V-I) = (19.7, 0.95)$ from those authors. We thus conclude that both photometries agree within the uncertainties.

DOLPHOT was employed again, this time in the artificial-star mode. Using fake-star experiments, we determined completeness as a function of magnitude, colour and position in the cluster, $c(m_{\rm F606W}, m_{\rm F606W} - m_{F814W}, R)$. The task ACSFAKELIST was used to generate artificial stars together with a Perl script. They were generated within

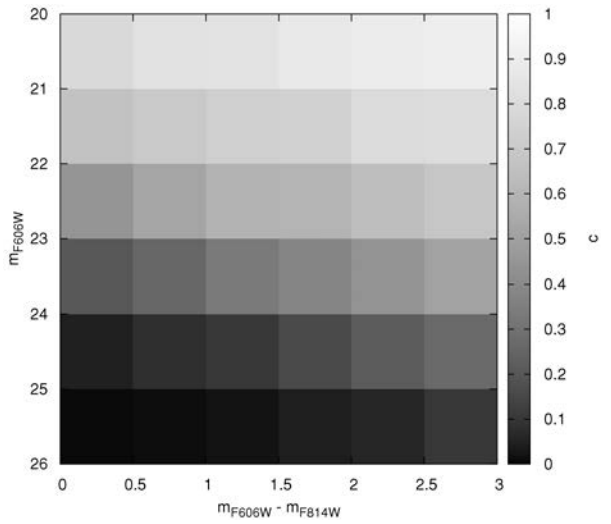

Figure 2. The position integrated completeness, $c(m_{\rm F606W}, m_{\rm F606W} - m_{\rm F814W})$ plotted over the CMD plane. The colour dependence is clear.

the ranges $20 \leq m_{\rm F606W} \leq 27$ mag and $0 \leq (m_{\rm F606W} - m_{F814W}) \leq 2.5$. We adopted bin sizes of 1 mag in $m_{\rm F606W}$, 0.5 mag in $(m_{\rm F606W} - m_{F814W})$ and 100 pixels in distance from the cluster centre. The number of stars generated in a single realization of the experiment was never larger than 10 per cent of the total original number in each region of the image. To build statistics, we performed three experiments for each $(m_{\rm F606W}, m_{\rm F606W} - m_{F814W}, R)$ bin. A total of $\sim 1.2 \times 10^5$ stars were generated. The images with artificial stars added underwent the same photometric and classification process as the original ones. As usual, c was taken as the ratio between the number of recovered artificial stars to the total. The result of the completeness analysis on the CMD plane is shown in Fig. 2, where we sum the results over all the radii. There is a strong colour dependence in the expected sense: at a fixed $m_{\rm F606W}$, redder stars have higher c values, since they are brighter (and therefore more easily detected) in $m_{\rm F814W}$.

3 ANALYSIS

3.1 Colour–magnitude diagram

Fig. 3 shows the CMD for the stars located within $r \leq 40$ arcsec ($\leq$1.6 pc) from the nominal centre of NGC 6642. By restricting the image region, we strongly reduce field contamination. The selected central region contains about 40 per cent of the total number of stars and only 10 per cent of the field area. Therefore, the vast majority of the stars in this field are expected to be GC members and should trace the evolutionary sequences of this object. In fact, we can see a well-defined structure in the main-sequence (MS) spanning $\approx$6 mag below the MSTO (located at $m_{\rm F606W} \simeq 19.2$). The subgiant branch (SGB), red giant branch (RGB) and HB are also clearly seen. Some candidate asymptotic giant branch (AGB) stars are also present. The top of the RGB and AGB is not well sampled due to saturation, even in the short exposures. The solid contour in the left-hand panel indicates our selected limits for these stellar evolutionary loci. The chosen limits also avoid effects of saturation and incompleteness. For instance, our cut-off at $m_{\rm F606W} \simeq 24.7$ at the CMD bottom avoids stars with completeness corrections $1/c > 3$. The open circles in the left-hand panel indicate BS candidates.

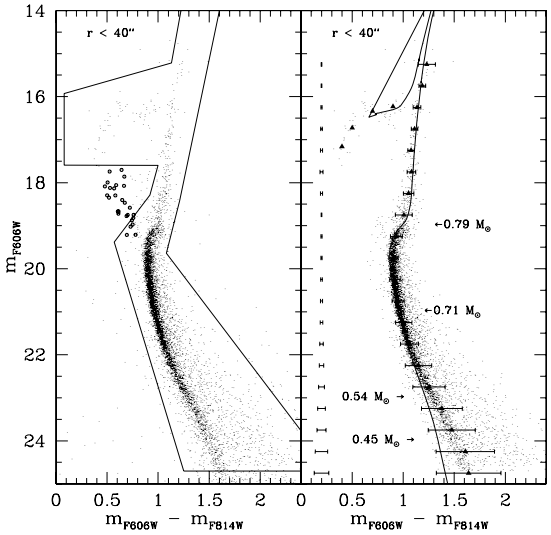

Figure 3. Left-hand panel: CMD of all sources that satisfy the DOLPHOT parameter cuts and which are located within $r \leq 40$ arcsec from the centre of NGC 6642. We also show the region used to select the cluster evolutionary sequences. The BS candidates are marked with open circles. Right-hand panel: same CMD as in the previous panel but cut is according to the selected region. The solid triangles show the CMD fiducial line and corresponding dispersion. The mean photometric error is shown in the extreme left of this panel. Some mass values are given along the MS. The best-fitting isochrone is over plotted and has the following parameters: log(age) = 10.14 (τ = 13.8 Gyr); [Fe/H] = −1.80; $E(B-V) = 0.46$; $(m-M)_0 = 14.55$.

In the right-hand panel of Fig. 3, the GC fiducial line is shown on top of the selected stars. The mean colour was calculated in magnitude bins for the MS, SGB and RGB. In the HB, the fiducial sequence was built by computing the mean magnitude in colour bins. The sequence is shown as solid triangles. We also show the dispersion around the fiducial points plus the mean photometric error for each magnitude bin. The photometric errors decrease with brighter magnitudes as expected up to $m_{\rm F606W} \simeq 19$. At yet brighter magnitudes, the uncertainties initially increase because the measurements come from the short ACS exposures, since the long ones saturate at these bright levels. The dispersion around the fiducial points is slightly larger than the associated photometric errors. This is mostly due to the fact that the mean photometric errors are calculated over the entire image, while the SGB and RGB stars are mainly located in the central region ($r \leq 40$ arcsec) of the cluster, where crowding effects are not negligible. At the lower MS, unresolved binarism plays a role in causing additional spread in colours. The dispersion of the fiducial line is larger near the bright end of the MSTO due to field stars and BS contamination. The NGC 6642 inner field CMD is used to visually fit isochrones. We use the isochrone grid computed[2] by Girardi et al. (2000) for that purpose. We also allow for variations in $E(B-V)$ and $(m-M)_0$ in the fits. The best-fitting isochrone is shown in the right-hand panel of Fig. 3. The corresponding parameters are $\log[\tau({\rm yr})] = 10.14$ and [Fe/H] = −1.80, $E(B-V) = 0.46$ and $(m-M)_0 = 14.55$.

The best-fitting model describes most of the MS, including the MSTO, plus the SGB and RGB regions. A discrepancy is seen for $m_{\rm F606W} > 23$, in the sense that the best-fitting isochrone is too blue. This is likely the result of unaccounted opacity in the low-mass

[2] http://stev.oapd.inaf.it/cgi-bin/cmd

Padova models (Baraffe et al. 1998). The model HB is too short compared to the data, probably reflecting the model uncertainties at this evolutionary stage. The best fit we find is a compromise between the two discrepancies just mentioned. For instance, in order to fit the cluster lower MS, a lower age must be used, but this eliminates the HB in the model, as we just mentioned. On the other hand, to better fit the HB, a very low metallicity must be adopted, which jeopardizes the fits to the other loci and also is in clear conflict with the spectroscopic metallicity determination by Minniti (1995).

In order to determine parameter uncertainties and to test our visual fit, we generated model cluster fiducial lines and compared them with the observed one, shown in the right-hand panel of Fig. 3. The models incorporated the effect of unresolved binaries, assuming a typical mass ratio of $m_2/m_1 = 0.5$ and binary fraction of 50 per cent. A χ^2-like statistic was adopted in search of the best model, and the parameter uncertainties were taken as the parameter range that satisfy the criterion $\chi^2_{\rm min} \leq \chi^2 \leq 2\chi^2_{\rm min}$. This approach led to the following results: $\log[\tau({\rm yr})] = 10.14 \pm 0.05$ and $[{\rm Fe/H}] = -1.80 \pm 0.2$; $E(B-V) = 0.46 \pm 0.02$ and $(m-M)_0 = 14.53 \pm 0.18$. We thus confirm the parameters of NGC 6642 using two different methods.

3.2 Alternative age estimate

In this section, we explore an alternative way to constrain the age of NGC 6642. A consistency check on the estimated age is obtained from the magnitude difference between the HB and the MSTO, $\Delta V^{\rm TO}_{\rm HB}$. We here adopt the same parametrization of this quantity as a function of [Fe/H] and τ as used in Glatt et al. (2008), which originally comes from Walker (1992):

$$\log\tau({\rm yr}) = -0.045[{\rm Fe/H}] + 0.37\Delta V^{\rm TO}_{\rm HB} - 0.24. \quad (1)$$

We estimate the HB and MSTO magnitudes as $V_{\rm HB} \simeq 16.25$ and $V_{\rm TO} \simeq 19.75$, respectively. Note that the HB in special has a considerable scatter around the quoted value. Assuming these values, we obtain $\Delta V^{\rm TO}_{\rm HB} = 3.5$, yielding in turn an age $\tau = 13.7$ Gyr. This estimate is consistent with that resulting from isochrone fitting.

3.3 Density profiles

To analyse the density structure of NGC 6642, we computed the RDP. Stars at various radii are weighted by the inverse of their completeness and their projected spatial density is obtained. The annuli used for the RDP construction were the same as in the completeness analysis.

Building a meaningful RDP, however, requires some cautionary steps. One is finding out the cluster centre, which is determined by the following method: (i) we count stars along the x-axis and (ii) the peak of this distribution is then assumed to be the x coordinate of the centre. The same procedure is then applied to the y-axis. For a spherical distribution, this procedure clearly yields the centre of the distribution of stars, which may also be assumed to be approximately the centre of mass. The adoption of alternative methods shows that our centre determination is robust.

Another important issue is the effect of field boundaries. They cause areal completeness effects at the outer radial bins, which had to be taken into account in the density estimates. For that purpose, we applied a Monte Carlo integral to find out the fraction of the total area in each bin which was effectively sampled by the image. Note that in the proximity of the image boundary the error associated to the density estimate grows significantly due to the increased loss of areal sampling.

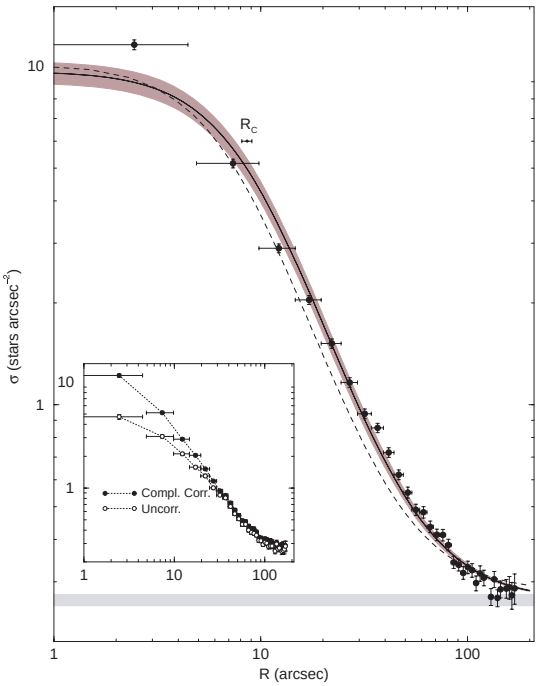

Figure 4. The RDP of NGC 6642. We include only stars with $m_{\rm F606W} \leq 24$. The filled circles show the completeness-corrected number density profile, as given by equation (2). The horizontal bars show the radial range of each bin. A King-like profile fit is shown as the solid line. The grey region is bracketed by the profiles resulting from varying the best-fitting parameters by $\pm 1\sigma$. The dashed line is the best-fitting profile assuming a higher value for the background star number density. The inset compares the completeness-corrected profile (solid points) with the uncorrected profile (open symbols).

At each radius, the density of stars was given by

$$\sigma(r) = \frac{\sum_i 1/c_i}{A(r)}, \quad (2)$$

where the sum above takes place over all stars located within the annulus of radius r, whose effective area (corrected for image boundary) is $A(r)$. Each star is weighted by the inverse of its associated completeness c value, as estimated according to the procedure described in Section 2.

The resulting RDP is given as the solid circles in Fig. 4. The horizontal bars correspond to the radial bin size. The solid line is the best-fitting King profile (see below). The 1σ uncertainty range is also shown, as the grey region. In the inset, we show the RDP that results from counting all stars with the same weight (therefore not corrected for completeness). Clearly, completeness corrections are crucial, especially in the central and denser regions, making the RDP much steeper than the uncorrected one. The completeness-corrected RDP has no evidence for a core-like flattening. A fit to a King-like profile yields $r_{\rm core} = 8.6$ arcsec and $\sigma(0) = 9.4 \pm 0.7$ stars arcsec^{-2}. The best-fitting central density, however, is substantially lower than the observed one. Changing the density of field stars in the fit does not alter this conclusion. We thus conclude that NGC 6642 is in fact a core-collapsed GC.

Using the inner field CMD shown in Fig. 3, we can visually identify some BSs. The number of candidate BS stars, as selected from their CMD position, is 50 per cent higher in the GC region

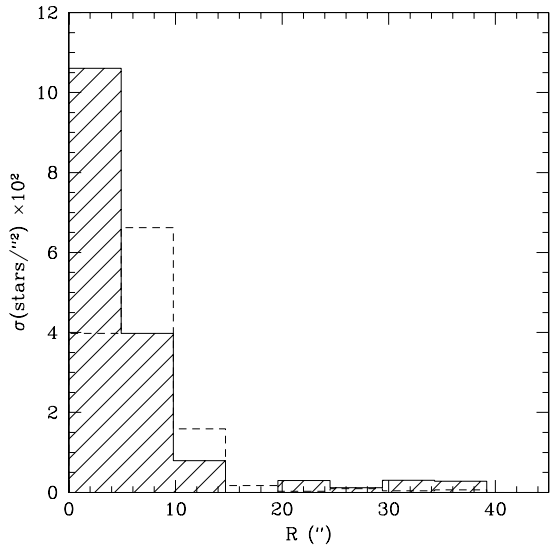

Figure 5. The density profile of selected BS (solid histogram) and HB (dashed histogram) stars, showing that most of the BSs are located in the inner region of NGC 6642. The BS population is more peaked than that of the HB stars.

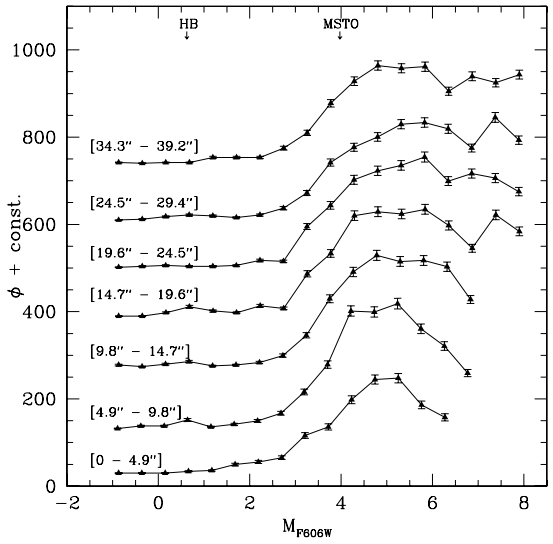

Figure 6. The LF of NGC 6642 stars at different radii, as indicated next to each curve. The positions of the MSTO and HB are indicated on the top. An offset was added to each curve to avoid overlap among them. In the inner regions, the completeness function falls off more rapidly as a function of magnitude, yielding a brighter cut-off limit.

than in the general field. As the GC region represents only 10 per cent of the total image, the excess of BS candidates per unit area is a factor of $\simeq$15 higher than the field. This unequivocally shows that these stars have a high probability of being cluster members.

BSs are known to be strongly concentrated towards the centre in most GCs, adding support to their possible origin from mergers of cluster stars or coalescence of tightly bound binaries. For the spatial study of the BS candidates, we adopted the HB population as a comparison set. By doing so, we eliminate the dynamical effects over the spatial distribution of stars since HB stars have a mass similar ($m_{\rm HB} \simeq 0.80\,{\rm M}_{\odot}$) to the mass of the turn-off stars.

In Fig. 5, we show the density distribution of BS and HB stars as a function of distance from the GC centre. The BS stars are in fact strongly concentrated towards the inner region of NGC 6642. This highly concentrated BS distribution is the rule in GCs, with the possible exceptions of NGC 2419 and ω Cen (Ferraro et al. 2006; Dalessandro et al. 2008a). These latter two, however, are atypical as GCs in many aspects, showing evidence for a complex star formation history and very large unrelaxed cores (Norris, Freeman & Mighell 1996; Sollima et al. 2005; Bellazzini 2007). The distribution in Fig. 5 also shows a region entirely depleted of BS candidates ($15 < R < 20$ arcsec) followed by a residual population further out. This is consistent with what has been observed in most GCs as discussed by Dalessandro et al. (2008b).

3.4 Luminosity and mass functions

In this section, we study the distribution of stars as a function of luminosity and mass. These are important tools to assess dynamical effects, such as mass segregation and stellar evaporation, that take place throughout the GC lifetime.

The luminosity function (LF) is computed in the same radial bins as in the previous section. As in the case of RDPs, the LF is obtained by summing over stars in a given annulus, but this time also as a function of absolute magnitude $M_{\rm F606W}$, as follows:

$$\phi(M_{\rm F606W}) = \frac{{\rm d}N}{{\rm d}M_{\rm F606W}} = \frac{\sum_i 1/c_i}{\Delta M_{\rm F606W}}. \quad (3)$$

The sum above is carried out over all stars in the annulus whose absolute magnitudes are within the bin around $M_{\rm F606W}$ with width $\Delta M_{\rm F606W}$. The $M_{\rm F606W}$ values were computed by using the reddening and $(m - M)_0$ derived in Section 3.1. Note that we again weight stars according to the completeness function.

Fig. 6 shows the resulting LFs at different radial annuli. $\Delta M_{\rm F606W} = 0.5$ as adopted as bin size. A constant offset was added to the curves to avoid cluttering. Poisson error bars are also shown. The LFs extend towards fainter magnitudes at large radii because the completeness levels are higher at these lower density regions. Fig. 6 includes evolved stars as well as MS ones. The most striking variation in the LF shapes occurs in the MS domain ($M_{\rm F606W} > 3.5$), where the LF is clearly depleted of low-luminosity stars and has a clear peak in the inner cluster regions. In contrast, the outer regions display flatter LFs all the way to the detection limit.

An alternative way to look for mass segregation is to compute the present-day mass function (PDMF) from the observed LF. We use the best-fitting Padova isochrone to convert stellar luminosities into initial masses. Only stars below $m \simeq 0.8\,{\rm M}_{\odot}$ are considered in this conversion, since according to the model mass loss is more pronounced at higher masses, signalling evolutionary stages later than the MS. We then bin stars as a function of initial mass. The resulting PDMFs are shown, again for the different radial annuli, in Fig. 7. A constant offset was again added for clarity. The star counts are normalized to unit solar mass intervals. Mass segregation now stands out more clearly, as the PDMF is systematically steeper in the central regions of NGC 6642. More striking, however, is the fact that the number of stars decreases towards lower masses, in contrast to most observed PDMFs. Assuming an initial mass function (IMF) with a power-law behaviour, $\xi \propto m^{\alpha}$($\alpha = -2.35$ for a Salpeter IMF), the observed PDMF in NGC 6642 is evidence that this GC has lost most of its low-mass stars to the field. In order to quantify the slope of the observed PDMFs, we carry out power-law fits to the curves shown in Fig. 7. The resulting slopes α are shown in Table 1.

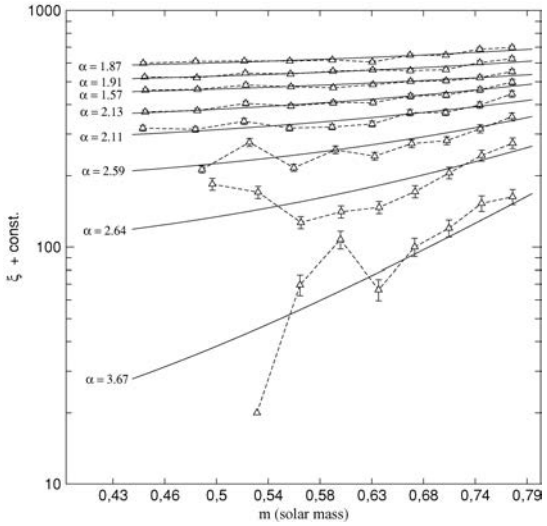

Figure 7. PDMFs for different annuli around the centre of NGC 6642. Distance from cluster centre increases upwards. We use the same radial bins used for the LFs. A constant offset was added to the star counts to avoid confusion. Fits to a power-law PDMF are also shown and the corresponding slope values are given. They are also listed in Table 1.

Table 1. Results of the power-law fitting to the MF at different radii.

$\Delta\, r$ (arcsec)	$m(\mathrm{M}_\odot)$	α
0–4.9	0.56–0.78	3.67 ± 0.93
4.9–9.8	0.53–0.78	2.64 ± 0.88
9.8–14.7	0.52–0.78	2.59 ± 0.60
14.7–19.6	0.45–0.78	2.11 ± 0.41
19.6–24.5	0.45–0.78	2.13 ± 0.21
24.5–29.4	0.45–0.78	1.57 ± 0.23
29.4–34.3	0.45–0.78	1.91 ± 0.26
34.3–39.2	0.45–0.78	1.87 ± 0.36

Note. Column 1 lists the radial bin in arcseconds, Column 2 gives the selected mass limits for the analysis and Column 3 shows fitted slopes α.

Note again the clear evidence for mass segregation, with a PDMF much more depleted of low-mass stars in the central regions.

We should point out that this inverted PDMF slope has been observed in other recent studies. Andreuzzi et al. (2001) found a power-law slope $\alpha \simeq 0.9$ for NGC 6712 for masses $m \leq 0.8\,\mathrm{M}_\odot$ and argue that this GC is very vulnerable to tidal disruption. De Marchi & Pulone (2007) also find a PDMF with decreasing number of stars at lower masses ($\alpha \simeq 0.5$, in the range $0.2 \leq m/\mathrm{M}_\odot \leq 0.8$) in NGC 2298. Finally, Paust et al. (2009) obtain a PDMF that peaks near the MSTO in NGC 6366.

Simulations of GC (Baumgardt & Makino 2003) show that in tidal fields the preferential depletion of low-mass stars leads to a PDMF with inverted slope when the cluster has undergone 90 per cent or more of its associated dissolution time. The time-scale associated with the slope inversion phenomena is related to the time when the compact stellar remnants start to dominate the cluster mass. Since NGC 6642 is a very old GC that resides in a central region of the Galaxy, the shape of the PDMF can easily be understood in the context of tidal interactions.

3.5 Horizontal branch morphology

We here determine the HB morphology using the parametrization described in Lee, Demarque & Zinn (1994):

$$\mathrm{HB}_{\mathrm{index}} = \frac{B - R}{(B + R + V)}, \tag{4}$$

where B is the number of stars in the blue part of the HB, R is the number of stars in the red part and V is the number of variable stars. To determine the colour of the RR-Lyrae instability strip, we used the HB analysis of the halo GC NGC 4147 by Stetson (2005). This cluster has a [Fe/H] very similar to NGC 6642. Stetson (2005) lists mean *BVI* magnitudes and colours for a sample of well-known RR-Lyrae in NGC 4147. We used the full range of mean colours as the instability strip. Our photometry was converted to the standard system by means of the transformations from Sirianni et al. (2005). The resulting index is then $\mathrm{HB}_{\mathrm{index}} \simeq 0.25$.

An alternative approach to determine $\mathrm{HB}_{\mathrm{index}}$ is to use the colour range of the instability strip quoted by Mackey & Gilmore (2004), based on the work of Smith (1995) and on the data from Piotto et al. (2002). These limits are in $(B - V)$ and were converted to $(V - I)$ using colour–colour transformations from Caldwell et al. (1993). The result is then $\mathrm{HB}_{\mathrm{index}} = 0.23$. This is in close agreement with the previous estimate. We use the uncertainties of 0.02 mag in the stability strip limits quoted by Mackey & Gilmore (2004) and propagate them into $\mathrm{HB}_{\mathrm{index}}$. Our final result is then $\mathrm{HB}_{\mathrm{index}} = 0.23^{+0.05}_{-0.01}$. This value is in apparent disagreement with that calculated by Mackey & Gilmore (2004) for NGC 6642 using the same limits but applied to the published CMDs from Piotto et al. (2002): $\mathrm{HB}_{\mathrm{index}} = -0.04 \pm 0.14$. This discrepancy, however, is dominated by the different reddening corrections adopted. We use $E(B - V) = 0.46$ whereas Piotto et al. (2002) find $E(B - V) = 0.41$. A lower $E(B - V)$ systematically shifts the entire HB towards redder intrinsic colours. This certainly yields a lower index. If we adopt this smaller $E(B - V)$ value to correct our observed HB and again apply the same colour range as Mackey & Gilmore (2004), we obtain $\mathrm{HB}_{\mathrm{index}} = 0.05^{+0.07}_{-0.09}$.

With $\mathrm{HB}_{\mathrm{index}}$ at hand, we may plot NGC 6642 in the HB-type versus metallicity diagram. Mackey & Gilmore (2004) use [Fe/H] $= -1.35$ for NGC 6642 and place it as a member of the young halo subsystem, according to the classification of van den Bergh (1993). Our $\mathrm{HB}_{\mathrm{index}}$ and [Fe/H] estimates confirm this position as far as the HB morphology is concerned, displacing NGC 6642 even further from the old halo and disc/bulge loci as seen in Fig. 8. On the other hand, its age and position in the Galaxy suggest that NGC 6642 is more likely an inner halo than an outer bulge transition object.

4 DISCUSSION

We studied the GC NGC 6642 with ACS/*HST* imaging in the F606W and F814W bands using combined long and short exposures. The ACS/*HST* photometry employed here makes it possible to resolve stars well in the vicinity of the cluster's collapsed core.

From the GC CMD, we have derived an age of 13.8 ± 1.6 Gyr and [Fe/H] $= -1.80 \pm 0.20$. We also derived a colour excess of $E(B - V) = 0.46 \pm 0.02$ towards NGC 6642 and a distance from the Sun comparable to that of the Galactic Centre, $\mathrm{d}_\odot = 8.05 \pm 0.66$ kpc object. Given the direction of NGC 6642 on the sky, and assuming that the distance from the Sun to the Galactic Centre is $d_{\mathrm{C},\odot} = 8.0$ kpc, we conclude that NGC 6642 in fact currently occupies a very central position in the Galaxy, $D_{\mathrm{C,clus}} = 1.4$ kpc.

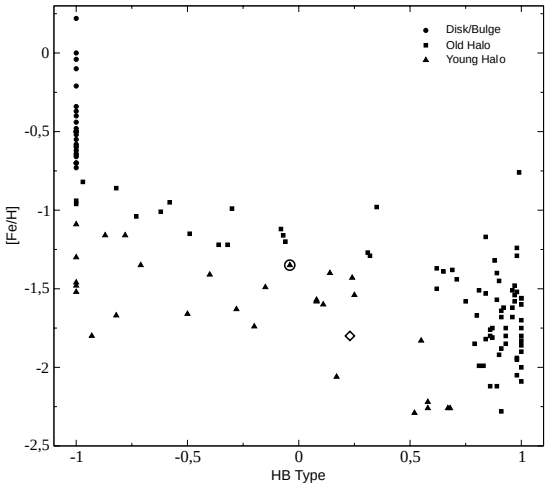

Figure 8. HB_{index} versus [Fe/H] diagram from Mackey & Gilmore (2004). Here, we show the old halo clusters (solid boxes),young halo clusters (solid triangles) and the disc/bulge clusters (solid circles). The solid triangle inside the open circle indicates the original position of NGC 6642 while the open diamond shows the position found in this work.

NGC 6642 has a very dense central core. Therefore, it is likely to be composed of stars that have undergone (or are undergoing) mergers. The very dense central object seen in Fig. 1 is not well resolved, although a high fraction of the BSs are found in its vicinity. The RDP shows no evidence of a well-resolved core, corroborating the idea that NGC 6642 is a core-collapsed GC.

A number of other surrounding BS candidates have been found. Their spatial distribution is more concentrated towards the GC centre than other GC stars, such as those in the HB. This result can also be interpreted in the context of the BS formation by merger scenario. We also observe a hint of bimodal RDP of the BS candidates, with a depletion region in the middle. These are common features in GCs (Dalessandro et al. 2008b).

The studied CMD also exhibits a well-developed HB from which we could estimate HB_{index} as defined in Lee et al. (1994). Along with the $\log[\tau(\mathrm{yr})]$ and [Fe/H] values found in this work, our analysis shows that NGC 6642 is an unusual GC. It has an old age and a central location in the Galaxy, but its position in the [Fe/H] and HB_{index} plane is more consistent with the young halo GC system. Having in mind its atypical behaviour concerning its dynamical evolution and HB morphology, NGC 6642 is more likely to be of a transition class between the inner halo and outer bulge cluster population.

The analysis of the LF and PDMF and their variation as a function of radius shows a clear evidence for mass segregation, especially in the range $0.4 \leq m/\mathrm{m}_{\odot} \leq 0.8$. Furthermore, in all regions, there is a decrease in the star counts towards lower luminosities and masses, an effect which is stronger in the central regions. This inversion in the PDMF slope is atypical, although it has been previously observed and is supported by dynamical *N*-body simulations (Andreuzzi et al. 2001; De Marchi & Pulone 2007; Paust et al. 2009). Our findings concerning the PDMF of NGC 6642, which resides in a violent environment, can be explained in terms of disc and bulge shocking through its perigalacticon passages (Baumgardt & Makino 2003). The high-resolution images available nowadays are allowing us to observe these phenomena more frequently and strongly suggest that dynamical effects over a GC lifetime have a dominant contribution from the external environment.

An interesting feature that is expected to result from the high degree of depletion of low-mass stars is the presence of a tidal tail around NGC 6642. For this purpose, a more sophisticated field decontamination technique must be adopted such as the statistical analysis of CMDs (Kerber et al. 2002). From the analysis of the RDP of NGC 6642, it is not clear that we have reached the tidal radius of the GC; thus, for the analysis of a possible tidal tail it is necessary to have images with a wider field. The tidal tail search could make the estimate of the mass loss due to tidal erosion possible.

ACKNOWLEDGMENT

This work was supported by Conselho Nacional de Desenvolvimento Científico e Tecnológico (CNPq) in Brazil.

REFERENCES

Aguilar L., Hut P., Ostriker J., 1988, ApJ, 335, 720
Andreuzzi G., De Marchi G., Ferraro F., Paresce F., Pulone L., Buonanno R., 2001, A&A, 372, 851
Baraffe I., Chabrier G., Allard F., Hauschildt P. H., 1998, A&A, 337, 403
Barbuy B., Bica E., Ortolani S., Bonatto C., 2006, A&A, 449, 1019
Baumgardt H., Makino J., 2003, MNRAS, 340, 227
Bellazzini M., 2007, A&A, 473, 171
Caldwell J., Cousins A., Ahlers C., van Wamelen P., Maritz E., 1993, SAAOC, 15, 1
Dalessandro E., Lanzoni B., Ferraro F., Vespe F., Bellazzini M., Rood T., 2008a, ApJ, 681, 311
Dalessandro E., Lanzoni B., Ferraro F., Rood T., Milone A., Piotto G., Valenti E., 2008b, ApJ, 677, 1069
De Marchi G., Pulone L., 2007, A&A, 467, 107
Dolphin A. E., 2000, PASP, 112, 1383
Ferraro F., Sollima A., Rood R., Origlia L., Pancino E., Bellazzini M., 2006, ApJ, 638, 433
Girardi L., Bressan A., Bertelli G., Chiosi C., 2000, A&AS, 141, 371
Glatt K. et al., 2008, AJ, 135, 1106
Harris W. E., 1996, AJ, 112, 1487
Ivanov V., Kurtev R., Borissova J., 2005, A&A, 442, 195
Kerber L., Santiago B., Castro R., Valls-Gabaud D., 2002, A&A, 390, 121
Lee Y. -W., Demarque P., Zinn R., 1994, ApJ, 423, 248
Mackey A. D., Gilmore G. F., 2004, MNRAS, 355, 504
Martin-Franch A. et al., 2009, ApJ, 694, 1498
Minniti D., 1995, A&A, 303, 468
Norris J., Freeman K., Mighell K., 1996, ApJ, 462, 241
Origlia L., Valenti E., Rich R., Ferraro F., 2005, MNRAS, 363, 897
Ortolani S., Bica E., Barbuy B., 2006, ApJ, 646, L115
Paust N. et al., 2009, AJ, 137, 246
Piotto G. et al., 2002, A&A, 391, 945
Richer H. et al., 2008, AJ, 135, 2141
Sarajedini A. et al., 2007, AJ, 133, 1658
Shin J., Kim S., Takahashi K., 2008, MNRAS, 386, L67
Sirianni M. et al., 2005, PASP, 117, 1049
Smith H., 1995, RR Lyrae stars. Camb. Univ. Press, Cambridge
Sollima A., Ferraro F., Pancino E., Bellazzini M., 2005, MNRAS, 357, 265
Stetson P. B., 2005, PASP, 117, 1325
Trager S. C., King Ivan. R., Djorgovski S., 1995, AJ, 109, 218
van den Bergh S., 1993, ApJ, 411, 178
Walker A., 1992, ApJ, 390, L81

This paper has been typeset from a TEX/LATEX file prepared by the author.

3 *LMC: candidatos à lacuna de idade*

A LMC é uma galáxia anã difusa do Grupo Local. Seu sistema de aglomerados é extremamente rico, com cerca de 900 aglomerados conhecidos. Este sistema nos dá acesso a tipos de aglomerados inexistentes na Galáxia, como por exemplo os globulares populosos, jovens e de alta metalicidade. Pela proximidade podemos estudar a população resolvida destes aglomerados da LMC, tendo assim uma visão precisa sobre o seu sistema de aglomerados.

Um dos mais intrigantes fatos sobre o sistema de aglomerados da LMC é a lacuna de idades. A lacuna foi inicialmente proposta por Jensen et al. (1988) como sendo a aparente ausência de aglomerados com idades entre 4 e 10 Gyr. A lacuna de idades também é visível na reconstrução do histórico de formação de aglomerados da LMC no trabalho de Parmentier et al. (2008). Apesar de fortes indicações de uma lacuna na formação estelar do ponto de vista da população de aglomerados, a reconstrução do histórico de formação estelar revela que existe uma população de campo com idade entre 4 e 10 Gyr (Javiel et al., 2005; Noël et al., 2007). A existência destas estrelas com idade consistente com a lacuna de idades pode indicar que a lacuna não se estende para aglomerados de baixa massa. Ou seja, se há uma população de campo com idades coerentes com a lacuna de idades ela deve ter origem em uma população de aglomerados que se dissolveu. No entanto, algum dos membros desta população deve ter sobrevivido até o presente e deveríamos ser capazes de observá-los.

O fato de haver apenas um aglomerado dentro da lacuna de idades de LMC pode ser uma consequência de um viés observacional com tendência a observar apenas aglomerados com alta massa. Aglomerados de alta massa são em geral mais brilhantes, de modo que são mais facilmente detectados. Portanto, uma maneira de testar as origens da lacuna de idades é sondar aglomerados de baixa massa cujas cores integradas são consistentes com a lacuna de idades.

Utilizando cores e magnitudes integradas, Hunter et al. (2003) estima a idade para 939 aglomerados da LMC. Dentre estes 939 aglomerados 4 possuem idades para pertencer à lacuna de idades. A técnica empregada por Hunter et al. (2003) não utiliza a população estelar resolvida de cada aglomerado, ao invés disso trabalha com a soma da luz de todas estrelas de um aglo-

merado. Esta técnica apresenta grandes vantagens ao lidar com um grande número de objetos. Porém, é incerta ao determinar as idades devido a degenerescência com a metalicidade e efeitos estocásticos introduzidos por estrelas brilhantes de campo (Girardi & Bica, 1993).

Uma maneira de melhorar as estimativas de idade é analisar a população estelar resolvida de cada aglomerado. De maneira similar ao que foi feito para NGC 6642 no capítulo anterior, podemos ajustar um modelo de evolução estelar e obter o melhor valor para a idade destes objetos. Utilizando dados do imageador óptico (SOI) instalado no *Southern Observatory for Astrophysical Research* (SOAR) - obtidos em duas noites de 2007, observamos a população estelar resolvida para os 4 candidatos à lacuna de idade de Hunter et al. (2003).

A determinação das idades destes candidatos à lacuna de idades foi feita através do ajuste de modelos de evolução estelar de Padova (Girardi et al., 2002). Por serem aglomerados de baixa massa, eles possuem poucas estrelas. Portanto, há necessidade de separar de maneira eficiente aquelas estrelas que pertencem ao aglomerado daquelas que pertencem à população de fundo da LMC. Essa separação é feita utilizando uma comparação estatística do CMD do aglomerado com o de população de fundo.

Apesar de ser adequado para separação de estrelas de campo em aglomerados relativamente pouco populosos, o método de comparação estatística do CMD, citado acima, apresenta problemas ao lidar com aglomerados extremamente pobres. Os aglomerados candidatos à lacuna de idade possuem entre 20-150 estrelas, o que pode ser um problema para os processos de descontaminação de estrelas de campo. Para contornar este problema nesse trabalho, desenvolvemos aprimoramentos às técnicas de descontaminação existentes. As modificações propostas aqui tem como objetivo lidar de uma maneira adequada com estatística de baixos números evitando o ruído conhecido como *shot noise*.

Neste capítulo apresentamos a redução dos dados do SOAR e a análise de 3 dos 4 aglomerados candidatos à lacuna de idades. Também introduzimos o método de descontaminação de estrelas de campo e o testamos em experimentos controlados, utilizando aglomerados de estrelas simulados. Além dos aglomerados candidatos à lacuna de idades, nos campos do SOI havia outros aglomerados já catalogados. Estes aglomerados foram analisados conjuntamente neste trabalho.

Monthly Notices of the ROYAL ASTRONOMICAL SOCIETY

Mon. Not. R. Astron. Soc. **404,** 1625–1632 (2010) doi:10.1111/j.1365-2966.2010.16390.x

Probing the Large Magellanic Cloud age gap at intermediate cluster masses

E. Balbinot,[1⋆] B. X. Santiago,[1] L. O. Kerber,[2] B. Barbuy[2] and B. M. S. Dias[2]

[1]*Departamento de Astronomia, Universidade Federal do Rio Grande do Sul, Porto Alegre, RS 91501-970, Brazil*
[2]*IAG, Universidade de São Paulo, São Paulo, SP 05508-090, Brazil*

Accepted 2010 January 20. Received 2010 January 11; in original form 2009 November 12

ABSTRACT

The Large Magellanic Cloud (LMC) has a rich star cluster system spanning a wide range of ages and masses. One striking feature of the LMC cluster system is the existence of an age gap between 3 and 10 Gyr. But this feature is not clearly seen among field stars. Three LMC fields containing relatively poor and sparse clusters whose integrated colours are consistent with those of intermediate-age simple stellar populations have been imaged in *BVI* with the Optical Imager (SOI) at the Southern Telescope for Astrophysical Research (SOAR). A total of six clusters, five of them with estimated initial masses $M < 10^4\,\mathrm{M}_\odot$, were studied in these fields. Photometry was performed and colour–magnitude diagrams (CMDs) were built using standard point spread function fitting methods. The faintest stars measured reach $V \sim 23$. The CMD was cleaned from field contamination by making use of the three-dimensional colour and magnitude space available in order to select stars in excess relative to the field. A statistical CMD comparison method was developed for this purpose. The subtraction method has proven to be successful, yielding cleaned CMDs consistent with a simple stellar population. The intermediate-age candidates were found to be the oldest in our sample, with ages between 1 and 2 Gyr. The remaining clusters found in the SOAR/SOI have ages ranging from 100 to 200 Myr. Our analysis has conclusively shown that none of the relatively low-mass clusters studied by us belongs to the LMC age gap.

Key words: stars: statistics – Magellanic Clouds – galaxies: star clusters – galaxies: stellar content.

1 INTRODUCTION

The Large and Small Magellanic Clouds (LMCs and SMCs, respectively) make up a very nearby system of low-mass, gas-rich and interacting galaxies. At their distances, both Clouds can be resolved into stars, allowing their stellar populations and star formation history (SFH) to be studied in detail. These studies open up the possibility of identifying epochs of enhanced or reduced star formation and of associating them with the system dynamics (Holtzman et al. 1999; Javiel, Santiago & Kerber 2005).

Star clusters provide an alternative tool to reconstruct the SFH of a galaxy. The Magellanic Clouds have a large cluster system, spanning a wide range of properties, such as masses, ages and metallicities, which, given their proximity, can be determined using different tools (Santiago 2009). Although they make up only a small fraction of the stellar mass in a given galaxy, star clusters have an advantage over field stars in that they may be modelled as simple stellar populations (SSPs), facilitating derivation of their main properties. Sizeable samples of clusters with available integrated magnitudes and colours currently exist. In the LMC, they have been used in association with evolutionary SSP models to derive age and mass distributions and to reconstruct the initial cluster mass function and the cluster formation rate (CFR; Hunter et al. 2003; de Grijs & Anders 2006; Parmentier & de Grijs 2008).

One striking and undisputable feature of the LMC cluster system is the so-called age gap. It was proposed by Jensen, Mould & Reid (1988) as a lack of clusters in the range $4 \leq \tau \leq 10$ Gyr. Several candidates to fill this gap were proposed and discarded since then (Sarajedini 1998; Rich, Shara & Zurek 2001). Evidence for the gap is present in the CFR reconstruction by Parmentier & de Grijs (2008). An age gap is also tentatively seen in some reconstructions of the LMC SFH based on field stars, although not systematically in all fields studied and not as clearly as in the cluster system (Javiel et al. 2005; Noël et al. 2007). The lack of a clear age gap among field stars suggests that it may be less pronounced among lower mass clusters ($M < 10^4\,\mathrm{M}_\odot$) as well, which tend to be systematically disfavoured in current magnitude-limited cluster samples in the LMC. Thus, the sample of candidate clusters with well-determined

⋆E-mail: balbinot@if.ufrgs.br

ages must be pushed towards fainter limits than has been previously done.

The most reliable cluster age determinations require CMD analysis. Confrontation of observed CMDs with theoretical ones, built from stellar evolutionary models, provides the best tool for age determination of single clusters, either with the *Hubble Space Telescope* or from the ground (Piatti et al. 2007, 2009; Baume et al. 2008). Building a cluster CMD, however, is a more costly task than obtaining integrated photometry, as it requires larger telescopes with high pixel sampling and good seeing conditions. Therefore, selection of candidates to fill the LMC age gap should be based on the aforementioned samples with integrated photometry. Furthermore, poor and sparse clusters suffer from more severe field star contamination on their CMDs, something that leads to a bias towards rich LMC clusters having detailed CMD analysis available.

In this paper, we analyse the CMDs of six LMC clusters for which no CMD is yet available. Two of these clusters have integrated colours consistent with an intermediate age, according to the photometry from Hunter et al. (2003). Five of them are sparse and inconspicuous when compared to previous samples. Our main goal is to probe relatively poor and intermediate-age clusters in search of possible examples that may have ages within the age gap. They have been imaged with the Optical Imager (SOI) at the Southern Telescope for Astrophysical Research (SOAR), under $\leq$1 arcsec seeing and with excellent point spread function (PSF) sampling. In Section 2, we describe the observations and photometry. In Section 3 we present our analysis tools, including a method to efficiently decontaminate the cluster CMD from field stars. This new decontamination method uses the entire information on the magnitude and colour space to subtract field stars from the CMD. We show the results for each cluster individually. In Section 4, we present our final discussion and conclusions.

2 DATA

The observations were made in a service mode and took place on the nights of 2007 November 10 and December 16, using the SOI in *B*, *V* and *I* filters. Fields were imaged around three LMC age gap candidates listed by Hunter et al. (2003):[1] OGLE-LMC0531, KMK88-38 and OGLE-LMC0169. Another field was observed around the richer and yet unstudied cluster NGC 1878. The field around OGLE-LMC0169 was observed under unstable and mostly bad seeing for our purposes, which led us to discard the data. For the remaining fields, the mean seeing was around 0.9 arcsec during both nights.

The SOI uses two 2050 $\times$ 4100 pixel CCDs, covering a 5.26 arcmin^2 field of view (FOV) at a scale of 0.077 arcsec pixel^{-1}. The images have a gap of 10.8 arcsec between the two CCDs. A slow readout was adopted in order to minimize detector noise. A 2 $\times$ 2 binning was used, yielding a spatial scale of 0.154 arcsec pixel^{-1}.

In Table 1 we summarize the observation log, where we show the target name, filter, seeing, number of exposures and exposure time. Multiple exposures were taken in order to increase the signal-to-noise ratio (S/N) and reject cosmic rays in the final combined image. For each cluster, a set of short exposures were also taken in order to avoid saturation of bright stars. The seeing is the mean full width at half-maximum of bright stars from the individual exposures. These exposures were flat-fielded, bias-subtracted, mosaicked and combined.

[1] The names OGLE-LMC, KMK88 and BSDL refer to Pietrzynski et al. (1999), Kontizas, Metaxa & Kontizas (1988) and Bica et al. (1999), respectively.

Table 1. Log of observations.

Target	Filter	Seeing (arcsec)	Exp. time (s)
OGLE-LMC0531	*B*	0.98	3 × 600
	V	0.85	3 × 200
	I	0.81	3 × 210
	B	0.91	2 × 20
	V	0.86	2 × 15
	I	0.77	2 × 10
KMK88-38	*B*	1.01	3 × 600
	V	1.01	2 × 200
	V	1.12	2 × 200
	I	0.91	3 × 210
	B	0.86	2 × 20
	V	0.86	2 × 15
	I	0.86	2 × 10
NGC 1878	*B*	1.31	3 × 600
	V	1.15	3 × 200
	I	0.85	3 × 210
	B	1.14	2 × 20
	V	1.05	2 × 15
	I	0.91	2 × 10

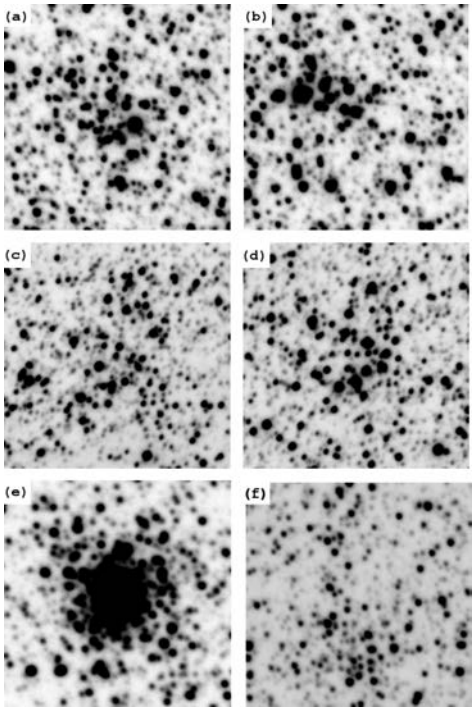

Figure 1. Sections of the final *V*-band images where the clusters are located. The size of each section is 50 $\times$ 50 arcsec^2. The cluster in each panel is as follows: (a) KMK88-38, (b) KMK88-39, (c) OGLE-LMC0531, (d) OGLE-LMC0523, (e) NGC 1878, (f) OGLE-LMC0214. In all figures, north is up and east is to the right.

The SOAR/SOI fields included three additional star clusters besides those taken from Hunter et al. (2003). They are OGLE-LMC0214, OGLE-LMC0523 and KMK88-39, respectively. The cluster names are taken from Hunter et al. (2003). Fig. 1 shows the sections (50 $\times$ 50 arcsec^2) of the final combined *V*-band images where the clusters are located. Five of them are low-density and relatively sparse open clusters; only NGC 1878 is a richer and more

compact object. To our knowledge, none of them has published CMD data in the literature.

For photometric calibration, two standard fields from Sharpee et al. (2002), located at the north-eastern arm of the SMC, were observed on each night. The observations have distinct airmasses ranging from 1.34 to 1.76. The magnitudes obtained from these images were used to fit a calibration equation for each passband (*B*, *V* and *I*). We took care to include standards covering a similar airmass range as the clusters and under seeing $\leq$1 arcsec. The fit residuals were $\sim$0.03 mag, indicating that both nights were photometric for most of the time.

Here we adopt a PSF fit photometry, the standard approach when dealing with crowded fields. The PSF model was computed using the images from the standard fields in order to avoid crowding effects on the PSF modelling. The photometry was carried out using DAOPHOT code from Stetson (1994). The photometry process took place as follows. (i) For each cluster, we chose the deepest and cleaner field for reference, usually the long exposure image on the *I* filter. Automatic detection of sources was carried out on this reference field using DAOFIND task, generating a master list of stars. (ii) This master list was then used as the position reference. (iii) The photometry on the remaining passbands then uses this master list, with only small positional offsets applied.

In Fig. 2, we show the residuals between the photometry of long and short exposures (hereafter *long* and *short*, respectively) for the cluster OGLE-LMC0531 as an example. It is clear that our photometry is accurate, since bright stars lie very near the zero residual line. Using this diagram we can determine the *long* saturation limit, where the residuals become negative. We can also determine the faint magnitude limit where the *short* S/N becomes small and the scatter in the residuals becomes larger. A systematic photometric offset of a few hundredths of magnitude was found between *short* and *long* and was interpreted as due to small seeing variations. They were dealt with by means of aperture corrections applied on the *short* magnitudes.

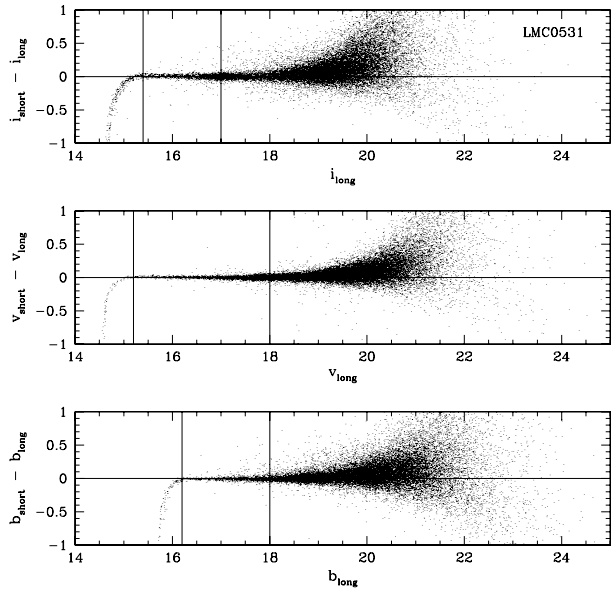

Figure 2. The residual diagrams for OGLE-LMC0531 in the *B* (lower panel), *V* (middle panel) and *I* (upper panel), where we show the difference between the instrumental magnitudes of the *long* and *short* images as a function of the *long* magnitude.

After photometric homogenization, we merge both *long* and *short* photometry tables. In essence, the merger process keeps only *short* stars brighter than the *long* saturation limit and only *long* stars fainter than the *short* low S/N limit. In the region between the quoted limits, we choose the star with the best magnitude measurement, i.e. the star with the smaller photometric error.

In Fig. 3, we show the result of the merging process. We also display the *long* saturation and *short* faint magnitude limits computed as previously described (solid lines). The CMDs display a characteristic shape, being dominated by the LMC fields stars, as expected, since our targets are intermediate-to-low-mass clusters. Moreover, we can distinguish the old and young population of the LMC divided by the extended Hertzsprung gap and can identify a very clear red giant branch (RGB) followed by the red clump (RC) and the asymptotic giant branch. On the blue side of the CMDs the main sequence (MS) extends to the domain of bright magnitudes, showing the presence of younger populations.

3 ANALYSIS

Since the clusters studied here are poorly populated objects, as shown in Fig. 1, it is crucial to differentiate the star cluster population from the field population. In fact, the field decontamination is the most challenging step in our analysis. For instance, KMK88-38 appears on the image as an excess of only $\sim$13 per cent relative to the same area in the field.

One popular method of decontamination is the statistical comparison of CMDs, such as the one developed by Kerber et al. (2002). In the literature, other methods are employed with success such as the statistical methods of Gallart et al. (2003), Bonatto & Bica (2007) and Piatti et al. (2008), and the proper motion analysis made by Richer et al. (2008).

3.1 Decontamination

The statistical method of Kerber et al. (2002) is based on the fact that the cluster population should appear as an overdensity in the colour–magnitude space (CMS) when compared against field stars. The decontamination is made by dividing the CMD into bins of colour and magnitude and then comparing star counts in each bin in the cluster region with the corresponding bin in the field region. This method deals with very sharp boundaries when counting stars, which leads to some shot noise when working with small numbers. The method uses a random process to select whether each star is a cluster member or not. This also leads to fluctuations on the final decontamination results.

An obvious improvement is to add an extra colour axis to the statistical field subtraction process. In this work, we explore two colours simultaneously and develop a method of decontamination that operates on the colour–colour–magnitude space (CCMS). To avoid sharp boundaries in the CCMS bins, each star is replaced by a three-dimensional Gaussian distribution with standard deviation equal to its photometric error. These additional features bring all the information available from the photometry into the analysis, using not only the position of the star in the CCMS but also its associated photometric error.

The cluster region and centre are determined by eye. Typical values for the cluster region radii are of $\sim$20 arcsec which correspond to a fraction of $\sim$1/60 of the SOAR/SOI FOV. In general, the clusters are too sparse and of low density to allow for a more systematic approach. We use all the remaining SOI area as the field region. For both the cluster and field regions, we take the following steps.

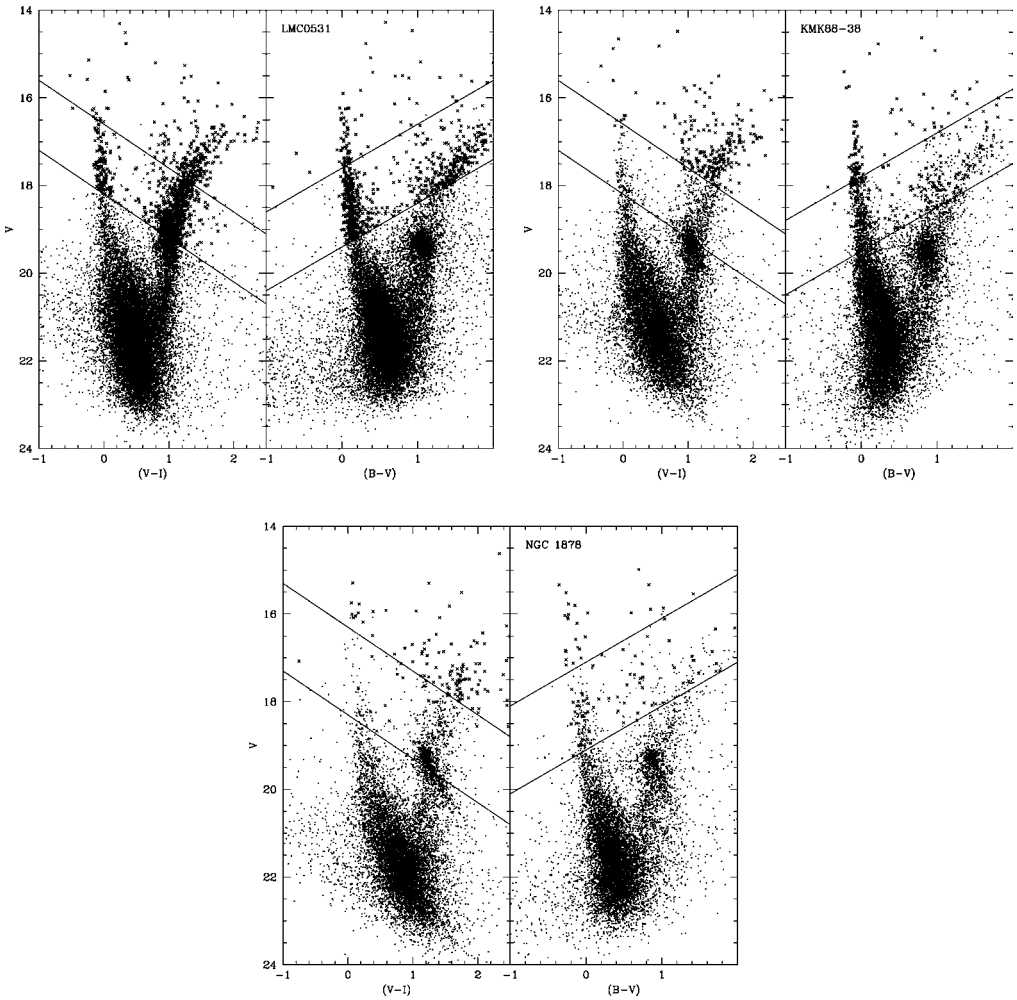

Figure 3. V, $(B-V)$ (right-hand panels) and V, $(V-I)$ (left-hand panels) CMDs from our sample. The combined *long* and *short* CMD for the entire SOI field is shown. The crosses are the stars that come from the *short* photometry and the black dots are from the *long* photometry. The upper solid line indicates the saturation limit and the lower line indicates the faint magnitude limit. The name of the cluster associated with the field is indicated in each panel.

(i) The CCMS is divided in a very fine grid of 0.01 in magnitude and 0.005 in both colours. (ii) For each bin we compute the contribution of each star by integrating its three-dimensional Gaussian over the bin volume. (iii) The resulting star counts in each bin are normalized by the different region areas.

After applying step (iii), we subtract the field star counts from the cluster ones at each bin. We then smooth out the resulting decontaminated cluster counts on CCMS by rebinning them on a coarser grid. For visualization purposes, we project the coarse CCMS grid on to the usual $(V-I)$, V and $(B-V)$, V CMD planes. The coarse grid size is chosen as the smallest possible that is able to evidence a population that resembles a SSP with minimal noise and acceptable resolution in the CMD plane. As we replaced a point process by smoothed three-dimensional Gaussians, the resulting CMDs were expressed in terms of star counts per bin.

3.2 Controlled experiments

In order to test the developed decontamination algorithm, we performed controlled experiments using artificially generated CMDs with parameters similar to those expected for the clusters in our sample.

To generate an artificial CMD, we used the aforementioned software developed by Kerber et al. (2002). This algorithm takes into account realistic photometric errors and the effects of CMD broadening due to unresolved binaries; the adopted binary fraction adopted here is 50 per cent.

We generated artificial CMDs for two isochrone models: one with $\log(\mathrm{age}) = 9.1$ and $Z = 0.010$ for which 50 stars were created and the other with $\log(\mathrm{age}) = 8.4$ and $Z = 0.010$ and containing 30 stars. 15 realizations of each model were created. Each artificial SSP realization is inserted into the real images at randomly chosen positions. By doing this we take into account effects caused by the stochastic nature of the artificial SSPs and the field.

In Fig. 4 we show the resulting decontaminated V, $(V-I)$ CMDs for the first eight of the 15 controlled experiments from the first isochrone mentioned above [$\log(\mathrm{age}) = 9.1$ and $Z = 0.010$, solid line]. The artificial stars generated are shown as crosses in all panels. The mean contrast relative to the field is 17 per cent. The parameters for this model are typical for the expected oldest clusters in our sample and should reflect the quality of the decontamination

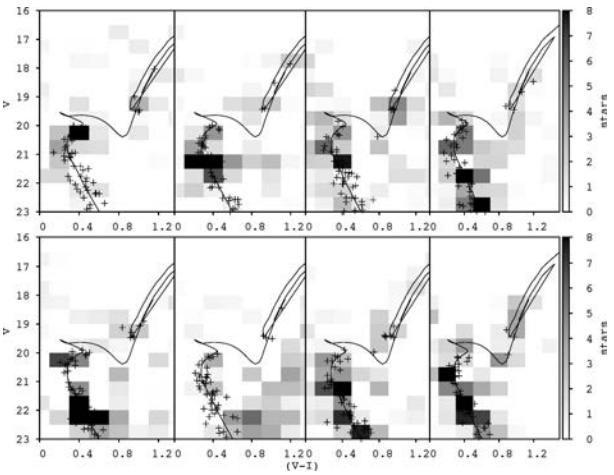

Figure 4. V, $(V - I)$ CMDs resulting from controlled experiments using an intermediate-age SSP with 50 stars. The employed isochrone is shown as the solid line in all panels. Its age is 1.25 Gyr and its metallicity is half the solar value. The artificially generated stars are shown as crosses. The field-subtracted star counts are coded with a grey-scale, which is shown as a colour bar on the right-hand side. The bin sizes in colour and magnitude are 0.2 and 0.5 mag, respectively.

algorithm for intermediate-age SSPs. We show only eight realizations of this experiment for simplicity.

Fig. 5 shows the results of the controlled experiment for the other isochrone model, with a younger age and same metallicity. The isochrone and artificial stars are again shown in all eight panels. The adopted age and metallicity [log(age) = 8.4 and $Z = 0.010$] are consistent with the youngest clusters in our sample. To test the method at yet lower contrast levels, only 30 stars were generated, yielding a mean contrast of 11 per cent.

The algorithm is successful in recovering the enhanced density contrast in the CCMS regions associated with the input SSP. Both the input MS turn-off (MSTO) and the RC positions can be identified in

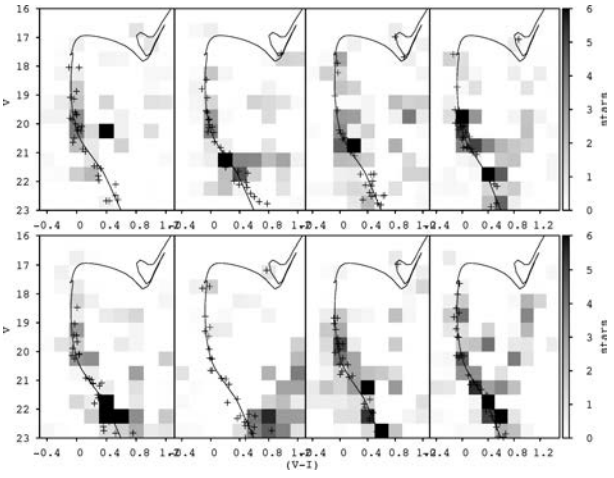

Figure 5. V, $(V - I)$ CMDs resulting from controlled experiments using a young SSP with 30 stars. The employed isochrone is shown in all panels as the solid line. It has an age of 250 Myr and a metallicity of half the solar value. The artificially generated stars are shown as crosses. The bin size and grey-scale representation of the field-subtracted star counts are the same as in the previous figure.

almost all realizations of the decontamination process applied to the first isochrone model (Fig. 4). The extended MS locus associated with the young SSP is also clearly visible in all but one of the panels of Fig. 5. The dense contaminating field and its associated fluctuations, however, often leave extra overdense CMD loci in some cases. In particular, in a couple of the realizations shown, the CMD is dominated by a faint and red plume of stars. This is likely caused by large and unaccounted photometric errors at these faint magnitudes and red colours. Considering that this plume is not associated with any reasonable SSP at the LMC distance, it can be easily discarded. More troubling is the residual field subgiant branch/RGB overdensity present in a couple of realizations shown in Fig. 5. This could make the age estimate an ambiguous task. On the other hand, addition of an extra colour, as is our case, helps us to remove this potential ambiguity. Also, in the vast majority of the realizations in both models, it is possible to identify the input SSP as the dominant excess of stars in the CMDs, on which isochrones may be visually overlaid in order to estimate their parameters.

3.3 Parameter determination

CMDs are widely used as a tool for parameter determination in the literature (Kerber, Santiago & Brocato 2007; Piatti et al. 2007), although there are alternative methods that can be employed in order to obtain similar results. These methods include integrated spectroscopy such as in Santos et al. (2006) and Ahumada et al. (2009), and integrated photometry as in Hunter et al. (2003) and Pessev et al. (2008).

Figs 6–8 show the CMDs that result from the decontamination process applied to our sample clusters. They can be used to extract physical parameters for the clusters. The target clusters are poorly populated, having typically from 20 to 150 stars. This limits the accuracy of the cluster parameter determination. Ideally, a statistical method based on CMD star counts should be used to infer ages, metallicities, distances and reddening. This has been done by several of the authors quoted in this paper. However, in the current case, we showed in the previous subsection that the fluctuation in the background field is the dominant source of noise in the decontaminated CMDs. As we cannot single out and eliminate a priori the contaminating field stars present in the cluster direction, the use of statistical methods for CMD comparison will not provide a significant advantage over isochrone fitting, as neither is capable of eliminating the effect of field contamination on the defined cluster region. This is a different situation from Balbinot et al. (2009) and Kerber et al. (2007), for instance, who used statistical CMD comparisons to infer parameters and their uncertainties for rich star clusters. Therefore, a visual isochrone fit is adequate to estimate cluster parameters in the present case. Isochrones come from the stellar evolutionary models by Girardi et al. (2002)[2].

We chose Padova isochrones although we are aware that systematic differences in the parameters may arise from the choice of one model or another. This issue has been investigated in more detail by Kerber & Santiago (2009), who compared different stellar evolution models applied to LMC clusters. They show that, in relation to Padova isochrones, the ones from BaSTI (Pietrinferni et al. 2004) tend to overestimate the age by ∼0.3 Gyr. PEL (Castellani et al. 2003) isochrones may lead to a discrepancy in the distance of ∼2.8 kpc at 50 kpc. The effects of convective overshooting (CO) are analysed in the same work. Obvious

[2] http://stev.oapd.inaf.it/cgi-bin/cmd

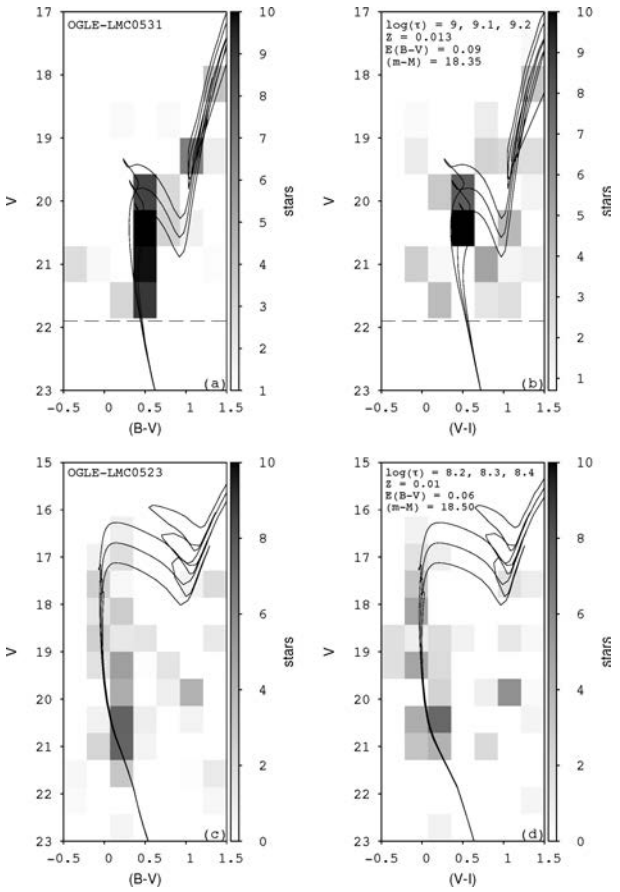

Figure 6. Panel (a): V, $(B-V)$ CMD of OGLE-LMC0531; panel (b): V, $(V-I)$ CMD for the same cluster as in the previous panel. The same model, whose isochrone parameters are indicated, was used on both CMDs. Panel (c): V, $(B-V)$ CMD of OGLE-LMC0523; panel (d): V, $(V-I)$ CMD for the same cluster as in panel (c). The same model, whose isochrone parameters are indicated, was used on both CMDs. In all panels, the field-subtracted star counts are coded with a grey-scale, which is shown as a colour bar on the right-hand side. The adopted bin size is 0.55 in magnitude and 0.30 in colour. The dashed line in the upper panels marks the position of the MSTO of a cluster with 3 Gyr and half solar metallicity.

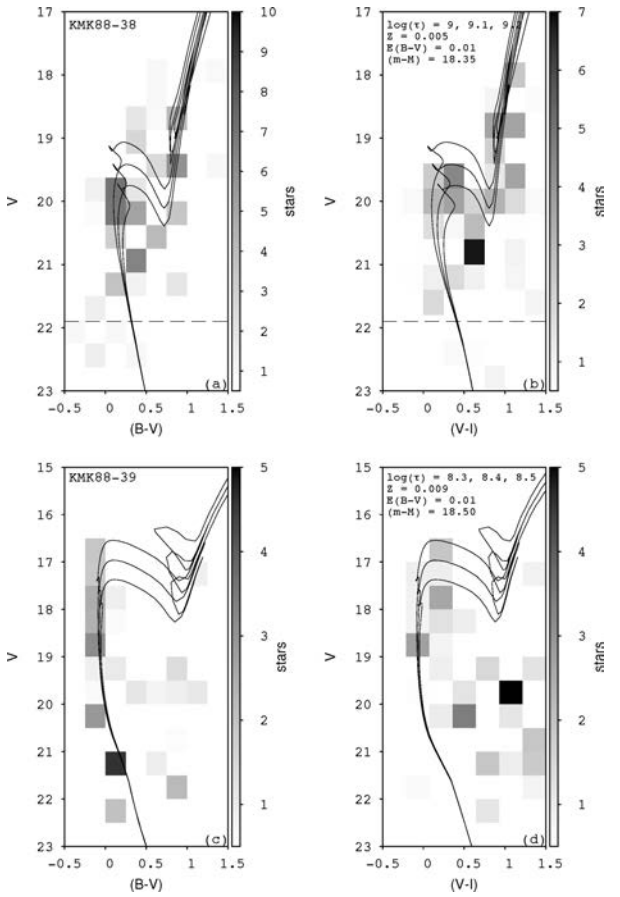

Figure 7. Same as in Fig. 6 but for the clusters KMK88-38 (panels a and b) and KMK88-39 (panels c and d). The adopted bin size is 0.40 in magnitude and 0.25 in colour.

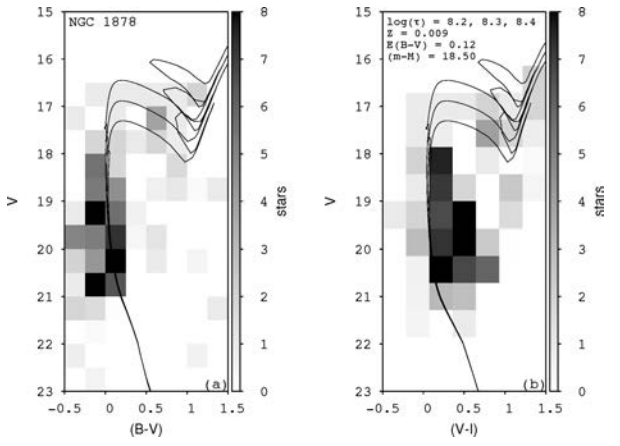

Figure 8. Same as in Fig. 6 but for the cluster NGC 1878. The adopted bin size is 0.50 in magnitude and 0.25 in colour.

differences in age arise between CO models and non-CO models, in the sense that the former yield an older age when compared to the latter $[\log(\mathrm{age})_{(\mathrm{CO})} - \log(\mathrm{age})_{(\mathrm{non-CO})} \simeq 0.1]$. Apart from that, however, Kerber & Santiago (2009) see no other significant trend in the parameters. The authors also compared their metallicity values with those obtained from spectroscopic data (Olszewski et al. 1991; Grocholski et al. 2006) and found that the Padova models give the best agreement between spectroscopic and photometric data. We thus conclude that, for the purpose of this paper, the influence of the model adopted is negligible and the differences from model to model are much smaller than the uncertainty of our parameter determination.

For each cluster, we derive the following parameters: age, metallicity, distance and colour excess. The parameters must obey some constraints in metallicity and distance, which are typical of LMC clusters. The allowed ranges adopted here are $18.25 \leq (m-M)_0 \leq 18.75$ and $(1/3)\,\mathrm{Z}_\odot \leq Z \leq \mathrm{Z}_\odot$ (Kerber et al. 2007). We take the reddening tables from Schlegel, Finkbeiner & Davis (1998) as an initial guess of $E(B-V)$. In some cases, the lack of clear CMD structures, such as the MSTO, RGB and RC, prevents strong constraints on the parameters, specially the distance modulus. In such cases, we keep it fixed at the mean LMC value.

The results of our parameter determination are listed in Table 2. We will now comment on the results for each cluster set. In Fig. 6–8

Table 2. The result of our CMD analysis. We list the object name, the derived log(age), metallicity, $E(B-V)$ and the distance modulus. The arrows indicate upper limits. The asterisk indicates where the distance modulus was fixed at the given value.

Name	log(age)	Z	$E(B-V)$	$(m-M)_0$
OGLE-LMC0214	8.4 ↓	0.013	0.10	18.50*
OGLE-LMC0523	8.3 ↓	0.010	0.06	18.50*
OGLE-LMC0531	9.1 ± 0.1	0.013	0.09	18.35
KMK88-38	9.1 ± 0.1	0.005	0.02	18.35
KMK88-39	8.4 ↓	0.009	0.01	18.50*
NGC1878	8.3 ± 0.2	0.009	0.12	18.50*

we show, along with the subtracted CMDs, three isochrones overplotted (solid lines). All isochrones have the same metallicity and only differ by age, whose values are given in the figures. In all the figures, the V, $(B-V)$ CMD is on the left-hand side and the V, $(V-I)$ is on the right-hand side. The cluster names and other isochrone fit parameters are also shown. All CMDs show star count in bins of colour–magnitude instead of stars themselves; the grey-scale is adjusted to minimize the noise and increase the contrast for better visualization.

3.3.1 OGLE-LMC0531 and OGLE-LMC0523

These two clusters are on the same SOAR/SOI field. Only the first one is an age gap candidate. As seen in Fig. 6, the two clusters have markedly distinct ages. In fact, OGLE-LMC0531 is older, with an age between ∼1 and 2 Gyr. No sign of an upper MS is seen in either the V, $(B-V)$ or the V, $(V-I)$ CMD. In the former, its MSTO and lower MS are more clearly defined, along with a trace of its RC. As explained earlier, this allowed better constraints on its physical parameters, yielding an $E(B-V) \simeq 0.09$, $(m-M)_0 = 18.35$ and a $Z = 0.013$. The extinction value is very similar to the initial guess taken from Schlegel et al. (1998).

OGLE-LMC0523 has an age of ∼200 Myr. In reality, this is an upper limit, since no clear turn-off is seen up to the saturation limits. Since no other clear CMD structure besides the MS is detected, it was harder to constrain the cluster distance. We adopted the mean LMC distance of $(m-M)_0 = 18.50$ and found $Z = 0.010$ and $E(B-V) \sim 0.06$.

3.3.2 KMK88-38, KMK88-39 and OGLE-LMC0214

KMK88-38 is our original target in this field, as an age gap candidate. The other clusters present in the field are KMK88-39 and OGLE-LMC0214. The latter was imaged only in the V and I bands, due to variations in telescope pointing. Even though we do not show its CMDs, it has been submitted to the same analysis as the other clusters, the results of which are shown in Table 2.

The field-subtracted CMDs for KMK88-38 and KMK88-39 are shown in Fig. 7. The panels and symbol conventions are the same as in Fig. 6. KMK88-38 is relatively old, with an age between 1 and 2 Gyr, similar to OGLE-LMC0531. The presence of strong CMD features, such as an MSTO, and an RGB allowed us to explore a wider range of parameters with the effect of better constraining their determination. The derived parameters for KMK88-38 are $(m-M)_0 = 18.35$, $Z = 0.005$ and $E(B-V) = 0.02$.

On the other hand, KMK88-39 is very young, with an age of ∼250 Myr when using a metallicity of $Z = 0.009$. The age derived for this cluster is again an upper limit, since no clear MSTO is seen. The distance adopted was again the mean LMC distance, and we found a reddening of $E(B-V) = 0.01$.

3.3.3 NGC 1878

NGC 1878 was accidentally observed in place of the age gap candidate cluster BSDL917. In contrast to the other fields, only one cluster was imaged this time. Even though an NGC object, NGC 1878 had never been studied before.

Since NGC 1878 is a relatively rich cluster ($\gtrsim$100 stars), it allowed us to explore our decontamination algorithm in a simpler case, where the density of cluster stars in the CMD at a given colour–magnitude bin is significantly greater than the noise generated by the fluctuation of field stars in this same bin. In Fig. 8 we show its subtracted CMD, adopting the same panels and symbols as in the two previous figures. We clearly see much more well-defined CMD loci than in the other cases, indicating that the decontamination process is effective.

The V, $(B-V)$ CMD of NGC 1878 looks slightly bluer than expected from the V, $(V-I)$ CMD. This means that a unique isochrone solution to both CMDs was harder to achieve. As a compromise, the best visual fit solution is slightly red (blue) when compared to the main MS locus in the former (latter) CMD. This effect can result from a combination of crowding and variable PSF, which may lead to increased light contamination on PSF fitting to the B band, therefore making the star seem bluer. The best isochrone fit gives a young age, ∼200 Myr, a typical LMC metallicity of $Z = 0.009$, $E(B-V) = 0.12$. We adopted a distance modulus of $(m-M)_0 = 18.50$.

4 CONCLUSIONS

We have obtained SOAR/SOI images of three fields containing six LMC clusters, two of which were previously identified as candidates to fill the LMC age gap. Photometry was carried out in three filters (B, V and I) reaching well below the MSTO of an old stellar population.

All but one of these clusters are poor and sparse, consistent with intermediate-to-low initial masses, requiring a careful and objective process to eliminate field stars from the cluster CMD. We developed such a method that simultaneously uses the information in the available three-dimensional space of magnitudes and colours. With the resulting decontaminated CMDs, we carried out visual isochrone fits based on Padova evolutionary sequences.

Our main result is that none of the clusters studied here is older than 2 Gyr, therefore not filling the LMC age gap. The two main candidates, OGLE-LMC0531 and KMK88-38, are in fact the oldest in the sample, displaying a clear MSTO and a branch of evolved stars. Their MSTO magnitudes are about 2 mag brighter than that expected for a 3 Gyr old SSP at the LMC distance, as evidenced from Figs 6–7. Interestingly, they are sided on the images by much younger clusters, for which only upper limits in age (<200 Myr) could be derived from the CMDs. This large age range is evidence either of a complex cluster formation history or of very efficient orbital mixing within the LMC. Another noticeable result is that the ages inferred here are similar to the last two close encounters between the LMC and SMC according to recent N-body simulations (Gardiner, Sawa & Fujimoto 1994), adding a few more examples of clusters that likely have formed as the result of SMC/LMC close-by passages. We also note that the two older clusters are systematically on the foreground relative to current models for the LMC disc (Nikolaev et al. 2004; Kerber et al. 2007).

The clusters in our sample are of lower initial mass ($M \sim 10^4\,M_\odot$) than most LMC clusters studied so far. The fact that they do not fill the age gap may indicate that yet lower mass clusters, possibly cluster remnants, must be sampled and studied in order to bridge the apparent inconsistency between reconstructed cluster and field star formation histories in the LMC.

ACKNOWLEDGMENTS

This work was supported by Conselho Nacional de Desenvolvimento Científico e Tecnológico (CNPq) in Brazil and Coordenação de Aperfeiçoamento de Pessoal de Nível Superior.

REFERENCES

Ahumada A. V., Talavera M. L., Clariá J. J., Santos J. F. C., Bica E., Parisi M. C., Torres M. C., 2009, in van Loon J. T., Oliveira J. M., eds, Proc. IAU Symp. 256, The Magellanic System: Stars, Gas, and Galaxies. Kluwer, Dordrecht, p. 293
Balbinot E., Santiago B. X., Bica E., Bonatto C., 2009, MNRAS, 396, 1596
Baume G., Noël N. E. D., Costa E., Carraro G., Méndez R. A., Pedreros M. H., 2008, MNRAS, 390, 1683
Bica E. L. D., Schmitt H. R., Dutra C. M., Oliveira H. L., 1999, AJ, 117, 238
Bonatto C., Bica E., 2007, MNRAS, 377, 1301
Castellani V., Degl'Innocenti S., Marconi M., Prada Moroni P. G., Sestito P., 2003, A&A, 404, 645
de Grijs R., Anders P., 2006, MNRAS, 366, 295
Gallart C. et al., 2003, AJ, 125, 742
Gardiner L. T., Sawa T., Fujimoto M., 1994, MNRAS, 266, 567
Girardi L., Bertelli G., Bressan A., Chiosi C., Groenewegen M. A. T., Marigo P., Salasnich B., Weiss A., 2002, A&A, 391, 195
Grocholski A. J., Cole A. A., Sarajedini A., Geisler D., Smith V. V., 2006, AJ, 132, 1630
Holtzman J. A. et al., 1999, AJ, 118, 2262
Hunter D. A., Elmegreen B. G., Dupuy T. J., Mortonson M., 2003, AJ, 126, 1836
Javiel S. C., Santiago B. X., Kerber L. O., 2005, A&A, 431, 73
Jensen J., Mould J., Reid N., 1988, ApJS, 67, 77
Kerber L. O., Santiago B. X., 2009, in van Loon J. T., Oliveira J. M., eds, Proc. IAU Symp. 256, The Magellanic System: Stars, Gas, and Galaxies. Kluwer, Dordrecht, p. 391
Kerber L. O., Santiago B. X., Castro R., Valls-Gabaud D., 2002, A&A, 390, 121
Kerber L. O., Santiago B. X., Brocato E., 2007, A&A, 462, 139
Kontizas E., Metaxa M., Kontizas M., 1988, AJ, 96, 1625
Nikolaev S., Drake A. J., Keller S. C., Cook K. H., Dalal N., Griest K., Welch D. L., Kanbur S. M., 2004, ApJ, 601, 260
Noël N. E. D., Gallart C., Costa E., Méndez R. A., 2007, AJ, 133, 2037
Olszewski E. W., Schommer R. A., Suntzeff B., Harris H., 1991, AJ, 101, 515
Parmentier G., de Grijs R., 2008, MNRAS, 383, 1103
Pessev P., Goudfrooij P., Puzia T., Chandar R., 2008, AAS Meeting, 211, No. 162.27
Piatti A. E., Sarajedini A., Geisler D., Gallart C., Wischnjewsky M., 2007, MNRAS, 382, 1203
Piatti A. E., Geisler D., Sarajedini A., Gallart C., Wischnjewsky M., 2008, MNRAS, 389, 429
Piatti A. E., Geisler D., Sarajedini A., Gallart C., 2009, A&A, 501, 585
Pietrinferni A., Cassisi S., Salaris M., Castelli F., 2004, ApJ, 612, 168
Pietrzynski G., Udalski A., Kubiak M., Szymanski M., Wozniak P., Zebrun K., 1999, Acta Astron., 49, 521
Rich R. M., Shara M. M., Zurek D., 2001, AJ, 122, 842
Richer H. B. et al., 2008, AJ, 135, 2141
Santiago B. X., 2009, in van Loon J. T., Oliveira J. M., eds, Proc. IAU Symp. 256, The Magellanic System: Stars, Gas, and Galaxies. Kluwer, Dordrecht, p. 69
Santos J. F. C. Jr, Clariá J. J., Ahumada A. V., Bica E., Piatti A. E., Parisi M. C., 2006, A&A, 448, 1023
Sarajedini A., 1998, AJ, 116, 738
Schlegel D. J., Finkbeiner D. P., Davis M., 1998, ApJ, 500, 525
Sharpee B., Stark M., Pritzl B., Smith H., Silbermann N., Wilhelm R., Walker A., 2002, AJ, 123, 3216
Stetson P. B., 1994, PASP, 106, 250

This paper has been typeset from a TEX/LATEX file prepared by the author.

4 *As caudas de maré do aglomerado NGC 2298*

A população de aglomerados globulares que vemos hoje na Via Láctea é apenas uma fração daquela que um dia existiu. Estes objetos perdem estrelas ao longo de sua existência através de uma variedade de mecanismos. Inevitavelmente a perda de estrelas leva à completa destruição destes aglomerados.

A dinâmica interna de um aglomerado globular é governada pela relaxação de dois corpos. Levando em consideração apenas os efeitos da dinâmica interna, um aglomerado levaria centenas de tempos de relaxação para evaporar completamente (Binney & Tremaine, 1987). Porém, um aglomerado não existe sem estar ligado a uma galáxia hospedeira. Esta galáxia perturba o potencial gravitacional do aglomerado acelerando o processo de dissolução (Spitzer & Thuan, 1972).

Quando um corpo extenso está sob influência de um campo gravitacional dependente da distância, ele está sobre a ação de uma força de maré. Isto faz com que a magnitude da atração gravitacional não seja a mesma em diferentes pontos deste corpo. Aglomerados globulares são corpos extensos orbitando o centro da Via Láctea. O campo de maré gerado pela Galáxia cria uma direção preferencial para que as estrelas escapem do potencial do aglomerado. A velocidade típica de uma estrela dentro de um aglomerado não excede os $\sim$ 10 km/s (nos casos mais extremos), enquanto a velocidade orbital do aglomerado é $\sim$ 200 km/s. Portanto, ao escapar a estrela compartilha aproximadamente a mesma órbita que o aglomerado. Aquelas estrelas que escapam pelo lado interno da órbita acabam ficando adiantadas e aquelas que escapam pelo lado externo ficam atrasadas em relação à órbita do aglomerado. Portanto, a trilha de estrelas que escapa do aglomerado traça aproximadamente a órbita dele. Utilizando diversas órbitas podemos criar vínculos fortes sobre o potencial da Via Láctea, mapeando com grande detalhe a distribuição de matéria na Galáxia.

Evidências desse processo de dissolução podem ser encontradas em aglomerados próximos, dentro de nossa Galáxia. Um dos casos mais marcantes é o aglomerado Palomar 5 que possui

longas caudas de maré que se estendem por mais de 15° no céu. No entanto, a detecção destas estruturas é extremamente desafiadora, pois a densidade superficial das caudas de maré normalmente é baixa (no halo temos ~ 1 estrela da cauda para cada ~ 100 estrela de campo). Apesar dos desafios, outras evidências de caudas foram encontradas utilizando uma ampla gama de métodos (Niederste-Ostholt et al., 2010; Sollima et al., 2011; Grillmair et al., 2006).

Neste trabalho buscamos desenvolver e testar uma implementação do método de *matched-filter* para detectar populações estelares esparsas sobrepostas a campos Galáticos. O método de *matched-filter* já foi extensivamente testado para detecção de caudas de maré, porém alguns aspectos de sua aplicação não foram cuidadosamente avaliados. Aqui buscamos testar o método em experimentos controlados onde simulamos um aglomerado de estrelas realístico, incluindo uma cauda de maré e efeitos observacionais (erros fotométricos e binarismo não resolvido). Esta cauda de maré simulada segue um perfil de densidade que decai com o inverso da distância.

Tendo uma implementação funcional e testada do método de matched-filter, prosseguimos para aplicação em um caso real. O aglomerado globular NGC 2298 foi observado durante uma noite utilizando o instrumento MOSAIC2 instalando no telescópio Blanco de 4 metros do Cerro Tololo International Observatory (CTIO). As observações cobrem cerca de 3 $graus^2$ atingindo magnitude $V \sim 23$. Esta magnitude equivale a uma massa estelar de 0.6 $M_\odot$ para um aglomerado à distância de NGC 2298. O raio de maré para este aglomerado é cerca de 8 *arcmin* (Harris et al., 1996), portanto nossas observações se estendem por dezenas de raios de maré. O grande campo de visão possibilita a procura por estruturas além do raio de maré e o modelamento preciso da população de campo.

O aglomerado NGC 2298 foi escolhido para este estudo porque possui uma função de massa invertida, assim como NGC 6642. Isto já é evidência de um alto grau de influência do meio sobre a evolução do aglomerado, tornando-o um bom candidato para a procura e caracterização das caudas de maré.

Neste capítulo apresentamos o desenvolvimento e teste de nossa implementação do *matched-filter*, assim como a análise fotométrica do aglomerado NGC 2298. O trabalho é apresentado sob forma de artigo científico, já submetido a revista *Monthly Notices of the Royal Astronomical Society*.

Mon. Not. R. Astron. Soc. **000**, 1–11 (0000) Printed 4 April 2011 (MN LATEX style file v2.2)

The tidal tails of NGC 2298

Eduardo Balbinot[1,2⋆], Basílio X. Santiago[1,2], Luiz N. da Costa[2,3], Martin Makler[2,4], and Marcio A. G. Maia[2,3]
[1] *Departamento de Astronomia, Universidade Federal do Rio Grande do Sul, Av. Bento Gonçalves 9500, Porto Alegre 91501-970, RS, Brazil*
[2] *Laboratório Interinstitucional de e-Astronomia - LIneA, Rua Gal. José Cristino 77, Rio de Janeiro, RJ - 20921-400, Brazil*
[3] *Observatório Nacional, Rua Gal. José Cristino 77, Rio de Janeiro, RJ - 22460-040, Brazil*
[4] *Centro Brasileiro de Pesquisas Físicas, Rua Dr. Xavier Sigaud 150, Rio de Janeiro, RJ - 22290-180, Brazil*

4 April 2011

ABSTRACT
We present an implementation of the matched-filter technique to detect tidal tails of globular clusters. The method was tested using SDSS data for the globular cluster Palomar 5 revealing its well known tidal tails. We also ran a simulation of a globular cluster with a tidal tail where we successfully recover the tails for a cluster at the same position and with the same characteristics of NGC 2298. Based on the simulation we estimate that the matched-filter increases the contrast of the tail relative to the background of stars by a factor of 2.5 for the case of NGC 2298. We also present the photometry of the globular cluster NGC 2298 using the MOSAIC2 camera installed on the CTIO 4m telescope. The photometry covers $\sim 3deg^2$ reaching $V \sim 23$. A fit of a King profile to the radial density profile of NGC 2298 shows that this cluster has a tidal radius of $15.91' \pm 1.07'$ which is twice as in the literature. The application of the matched-filter to NGC 2298 reveals several extra-tidal structures, including a leading and trailing tail. We also find that NGC 2298 has extra-tidal structures stretching towards and against the Galactic disk, suggesting strong tidal interaction. Finally, we assess how the matched-filter performs when applied to a globular cluster with and without mass segregation taken into account. We find that disregarding the effects of mass segregation may significantly reduce the detection limit of the matched-filter.

Key words: *(Galaxy:)* globular clusters: general; *(Galaxy:)* globular cluster:individual:NGC 2298; Galaxy: structure

1 INTRODUCTION

Globular clusters (GCs) are the oldest objects found in our Galaxy, hence they witnessed the early formation of the Milky Way (MW). Throughout the existence of a cluster, it looses stars by a series of both internal and external dynamical processes. To understand how stars formed inside a star cluster are delivered to the host galaxy is to understand a major part of the galaxy formation process in the hierarchical assembly paradigm. In that sense, the GCs that we see today are the reminiscent of a much larger population of building blocks of our Galaxy.

A GC may loose stars by a number of processes. Their internal dynamics, ruled by two-body relaxation, makes stars gradually leave the cluster and leads to their eventual dissolution in a time-scale of a few hundred relaxation times (Binney & Tremaine 1987). The external influence of the gravitational field of the Galaxy may accelerate the dissolution process (Spitzer & Thuan 1972). The external field has strong effects over the overall structure of the clusters. One of the most clear evidences of this influence is the existence of a limiting radius (Trager et al. 1995; King et al. 1968). Baumgardt & Makino (2003) showed that the presence of a tidal field throughout the evolution of a cluster results on dramatic changes on the mass function. This phenomenon was latter observed on several clusters (Andreuzzi et al. 2001; De Marchi & Pulone 2007; Balbinot et al. 2009) and is associated with clusters that are subject to extreme tidal interactions.

While orbiting the host galaxy, a GC experiences a slowly varying external potential, which has little effect on its structure, except when crossing the disk or bulge of the galaxy. On the crossing event the GC potential is rapidly changed, shrinking the tidal radius in a time-scale shorter than the cluster dynamical time, rapidly turning bound stars into unbound ones. This creates a preferential way of scape along the line of action of the tidal forces. Stars that leave through the inside of the GC orbit will leap forward in the

⋆ e-mail: balbinot@if.ufrgs.br

cluster path and stars on the outside will lag behind in the orbit. Since the velocity dispersion of the stars in the cluster is much less than the orbital velocity of the cluster, the stars that become loose follow approximately the same orbit. We may think of each unbound star as a test particle for the gravitational potential of the MW. Thus, by finding which orbit solution best fits the observed tail distribution, we may infer the best model for the MW potential (Koposov, Rix, & Hogg 2010).

The study of tidal tails necessarily requires a photometrically homogeneous dataset of a large number of stars to the faintest magnitudes possible. There were attempts to find tidal structures on several clusters using photographic plates (Leon, Meylan, & Combes 2000), finding only mild evidences of tidal structures in 20 GCs. More crucial to tidal tails analyses is the need of a large enough solid angle, since the tails may extend over tens of degrees on the sky. With the release of the Sloan Digital Sky Survey (SDSS; York et al. 2000), it was possible to investigate large areas of the sky with deep and accurate photometry. SDSS led to many discoveries such as tidal streams from disrupting satellite galaxies (Koposov, Rix, & Hogg 2010), new satellite galaxies (Walsh, Willman, & Jerjen 2009; Koposov et al. 2008), and tidal tails around GCs (Rockosi et al. 2002; Odenkirchen et al. 2003; Grillmair & Johnson 2006).

New large area photometric surveys are being planed for the near future. Among them is The Dark Energy Survey (DES). DES is a $5000deg^2$ photometric survey that will cover the southern galctic cap in five filters ($grizY$) (DePoy et al. 2008; Mohr et al. 2008). To achieve this area coverage DES will use a large field of view camera with an array of 64 high near infra-red efficient CCDs. This new instrument will be placed at the CTIO Blanco 4 meter telescope. DES will reach fainter magnitudes than SDSS with comparable area coverage. Although its primary goal is the determination of cosmological model parameters, a by-product of DES will be the sampling of stars from our Galaxy, which may have great impact over stellar population and Galactic structure studies (Rossetto et al. 2011).

In this paper, we develop and validate an implementation of the matched-filter technique to detect sparse simple stellar populations, such as GC tidal tails. We perform the validation on two controlled scenarios: (i) Realistic simulated GC plus a tidal tail; (ii) the halo globular cluster Palomar 5, which has a previously detected tidal tail. We then apply the algorithm to detect tidal structures on the halo globular cluster NGC 2298 which is believed to be a cluster on advanced stages of dissolution (De Marchi & Pulone 2007). Our ultimate goal is to apply the code that we present here to the entire DES sample and, as a consequence, obtain a homogeneous sample of such tidal features across the Southern sky. In Sect. 2 we describe the matched-filter method. In Sect. 3 we present the validation tests. In Sect. 4 we present the NGC 2298 data reduction and analysis of its structure and tail. In Sect. 5 we address the impact of mass segregation over the recovered tail from the matched-filter. In Sect. 6 we present our final discussion and conclusions.

2 MATCHED FILTER

The matched-filter (MF) is a long used technique developed for signal processing (Wiener 1949). The MF technique has a wide field of applications in astrophysics going from the detection of clusters of galaxies (Kepner et al. 1999) to the characterization of light curves of stars with eclipsing exoplanets (Doyle et al. 2000).

In this work, the MF is used to detect low-density simple stellar populations (SSP) that are projected against the Galactic field stars. This is done by determining the surface density of stars that are consistent with a given SSP by means of a weighted least-squares fit to a carefully constructed model. The implementations of the MF follow closely the work of Rockosi et al. (2002) and Odenkirchen et al. (2003). Although the MF has been well developed in these previous works, in this work we judge it necessary to redescribe the method in face of some additional features that we propose, which depend on the very definition of the functions and models adopted.

We want to detect a SSP overlaid with the Galaxy field populations. A simple model for the number of stars at a given position (α, δ) as a function of colour (c) and magnitude (m) may be written as:

$$N(\alpha, \delta, c, m) = n_{cl} + n_{bg} \quad (1)$$

where $n_{cl}$is the number of stars belonging the SSP and $n_{bg}$is the number of Galaxy field stars. n_{cl}can be obtained both from observational data or from simulations using known properties of this SSP (age, metallicity, redenning, distance, mass function, unresolved binary fraction and photometric errors).

n_{cl} may be normalized by the total number of stars that contribute to the SSP:

$$n_{cl}(\alpha, \delta, c, m) = \zeta_{cl}(\alpha, \delta) f_{cl}(\alpha, \delta, c, m) \quad (2)$$

where f_{cl}may be thought of as a probability function as in common statistics. In essence, f_{cl}describes the probability of randomly drawing a star from the SSP at a given colour and magnitude.

The same procedure may be applied to n_{bg}.

$$n_{bg}(\alpha, \delta, c, m) = \zeta_{bg}(\alpha, \delta) f_{bg}(\alpha, \delta, c, m) \quad (3)$$

A simple assumption here is to consider f_{cl}constant across all analysed field. This assumption bears some approximations with it. One of them is to consider the SSP at the same distance everywhere. Often the tail extends through *kpc* scales, which may lead to a variations on the distance modulus with position on the sky. A further approximation is to assume that the Present Day Mass Function (PDMF) from the cluster is the same as in the tidal tail. Baumgardt & Makino (2003) showed that dynamically evolved globular clusters have a rapidly evolving stellar mass function. So, the stars that are left along the tail may not be well described by the cluster PDMF, since these stars left the cluster on the past in an epoch when the mass function was different. This issue is further aggravated by mass segregation, since stars that leave the cluster are near its tidal radii, thus having a lower mass than the bulk of stars (Koch

et al. 2004). In this work, we initially drop the spatial dependency of f_{cl}, leaving an assessment of the impact caused by mass segregation to §5.

The number of Galaxy field stars is expected to vary slowly on large scales. This variation should be reflected on a position dependency on f_{bg}. The scale of the analysed field and its complexity will determine if the spatial dependence of f_{bg}may be disregarded or not. At each case a prescription of how the spatial variability was dealt with will be presented.

Considering all approximations quoted above, we are left with a simple model for the number of stars as a function of position, colour, and magnitude. This model assumes that there are only two stellar populations, the SSP itself and field stars from the Galaxy.

$$N(\alpha,\delta,c,m) = \zeta_{cl}(\alpha,\delta) f_{cl}(c,m) + \zeta_{bg}(\alpha,\delta) f_{bg}(\alpha,\delta,c,m) \quad (4)$$

The construction of $f_{cl}$and $n_{bg}$is done by means of a Hess diagram, where we divide the colour-magnitude diagram (CMD) in bins of 0.01 in colour and 0.1 in magnitude. The resulting diagram is then smoothed using a Gaussian kernel. We label the CMD bins by the index j. The sky is also divided in bins of right ascension and declination and labelled by the index i. For instance, $f_{bg}(\alpha_i, \delta_i, c_j, m_j)$ is the measure of f_{bg}at the i-th bin of spatial coordinates and the j-th CMD bin. From here on we use the notation $f_{bg}(i,j)$ for simplicity. Since these functions are now discrete functions of coordinates and CMD position, we must work with new discrete functions that are integrals over the CMD and solid angle bins. The discrete model for the number of stars is

$$N(i,j) = \gamma_{cl}(i) F_{cl}(j) + \gamma_{bg}(i) F_{bg}(i,j) \quad (5)$$

where

$$\begin{aligned} \gamma_{cl,bg}(i) &= \int_{\Omega_i} \zeta_{cl,bg}\ d\Omega \\ F_{cl}(j) &= \int_{P_j} f_{cl}\ dm\, dc \\ F_{bg}(i,j) &= \int_{\Omega_i}\int_{P_j} f_{bg}\ dm\, dc\, d\Omega \end{aligned}$$

where P_j is the area of the j-th pixel in the CMD and Ω_i is the solid angle covered by the i-th spatial bin.

Using this model for the number of stars in any region of the sky, we may now use an observed stellar sample and find the best fit to this model by means of a lest-squares fit. Let $n(i,j)$ be the observed distribution of stars. At the i-th position bin the quantity to be minimized is:

$$S^2(i) = \sum_j \frac{[n(i,j) - \gamma_{cl}(i)F_{cl}(j) - \gamma_{bg}(i)F_{bg}(i,j)]^2}{\gamma_{bg}(i)F_{bg}(i,j)} \ . \quad (6)$$

Minimizing equation (6) and solving for γ_{cl} (i.e. $\frac{dS^2}{d\gamma_{cl}} = 0$) we have:

$$\gamma_{cl}(i) = \frac{\sum_j n(i,j)F_{cl}(j)/F_{bg}(i,j)}{\sum_j F_{cl}^2(j)/F_{bg}(i,j)} - \frac{\gamma_{bg}(i)}{\sum_j F_{cl}^2(j)/F_{bg}(i,j)} \ . \quad (7)$$

In summary, one must plug in $n(i,j)$ on equation (7) to find the best estimate of γ_{cl}, which is in turn the best estimate of the number of stars that are consistent with the SSP. Equation (7) differs slightly from that found by Rockosi et al. (2002), although it matches exactly the one found by Odenkirchen et al. (2003). This discrepancy may be due to distinct definitions and model constructions.

Note that in equation (7) the denominator for both terms is constant at every position if we neglect the spatial dependency of F_{bg} (i.e. no i dependency). The number of background stars (γ_{bg}) can then be easily estimated from a polynomial fit to regions where we know for sure that there is no contribution from the SSP.

Our implementation of the MF was coded mostly using `Python`, with the aid of the `SciPy` module for signal processing routines. Some of the heavy array manipulation was carried out with Fortran and linked to `Python` using `F2Py`, which is part of the `Numpy` project. Despite being written in a high level language, our implementation does not require a great deal of computational power or time since most of the math is carried out by external routines which are written in C or Fortran (all the matched-filter analysis was carried out in a low-end desktop machine). We expect to release a public version of the code for the community through the Brazilian DES Science Portal in the near future.

3 VALIDATION TESTS

3.1 Simulations

To properly recreate the conditions where globular clusters are found (i.e. projected against a background of Galaxy field stars), we must be able to simulate field stars in any given direction of the sky. In addition, we must be able to generate realistic stellar populations from any given stellar evolution model, taking into account every observational effects. To achieve these goals a variety of softwares had to be employed.

The simulations of the Galaxy stars was done using the TRIdimensional modeL of thE GALaxy (`Trilegal`[1]) by Girardi et al. (2005). The `Trilegal` code simulates the stellar content of the Galaxy in any direction of the sky, including contributions from the four basic structural components: thin and thick disk, bulge, and halo. We refer to the original paper for further details on the code.

To simulate a globular cluster, we use an adaptation of the code from Kerber et al. (2002). The original code simulates the CMD of a stellar population for a given stellar evolution model, also taking into account the effects of unresolved binaries and observational errors. We modified the original code in order to include positions, by spreading the stars over the sky according to a given mass profile (e.g. King 1966?). In addition, a tidal tail is added using a $1/r$ density decay profile Johnston, Sigurdsson, & Hernquist (1999). Finally, we allow a position-dependent PDMF in order to incorpotate mass segregation effects.

We simulate a globular cluster located at $\alpha_{J2000} = 6^h48^m59^s$ and $\delta_{J2000} = -36^\circ00'02''$, which corresponds to the position of NGC 2298, analyzed in §4. Its structure is described by a King profile with a core radius $r_c = 0.91' =$

[1] http://stev.oapd.inaf.it/trilegal

2.8pc and a concentration parameter $c = log(r_t/r_c) = 0.94$. A Padova evolutionary model (Girardi et al. 2000) was chosen with $\log(age(yr)) = 10.10$ and $[Fe/H] = -1.98$. The simulated cluster is placed 10.8kpc away from the Sun with no reddening, for simplicity. We adopt a Kroupa IMF and choose not to include mass segregation. The adopted fraction of binaries for this simulations is of 50%. The tidal tails extend 1 kpc in each direction, with a position angle of 45° and an angle with the plane of the sky of 20°. The chosen tidal tails width is $16' = 50pc$. The simulated globular cluster has $\sim 2\,10^4$ stars with 20% of them belonging to the tidal tail. The simulation was carried out using the g and r passbands from DES.

A $20deg^2$ region of the Galaxy field stars was simulated using `Trilegal`. These stars were uniformly spread in a $24deg^2$ region around the simulated star cluster.

Photometric errors were added based on SDSS r magnitudes, which is consistent with a photometric detection limit of $r \sim 23.0$. This limit is also consistent with the observations of NGC 2298 (see §4.1 for details).

Since we know *a priori* which stars belong to the simulated cluster, it is fairly easy to build F_{cl} , the same is true for F_{bg} . We applied the MF to four tidal tails with different densities, 20% (3200), 10% (1600), 5% (800), and 1% (160) of the total number of simulated cluster stars. This was done by randomly removing stars from the simulated tail. Furthermore, we compared the MF results with a simpler method of quantifying the simulated tidal tail, based on simple star counts. In this alternative method we compute star counts at each spatial bin, evaluate the expected average background counts, and subtract this later from the former.

Figure 1 shows the on-sky distribution of simulated stars compared to the MF results. It is clear that the matched-filter improves the contrast of the tail relative to the field stars when compared to a direct star counting method. Yet, the comparison of the left and right columns in the figure reveal that the MF does not recover all the structure and extension in the tails, specially in the sparser cases. In figure 2 we compare, for the two methods, the resulting cluster counts to the actual number of simulated cluster stars. The matched-filter clearly reduces the noise in this scatter plot by a factor of 1.92/0.72 = 2.67, and therefore the contrast with the background, when compared to simple star counts method. We conclude that the our implementation of the matched-filter works well for this simulated set.

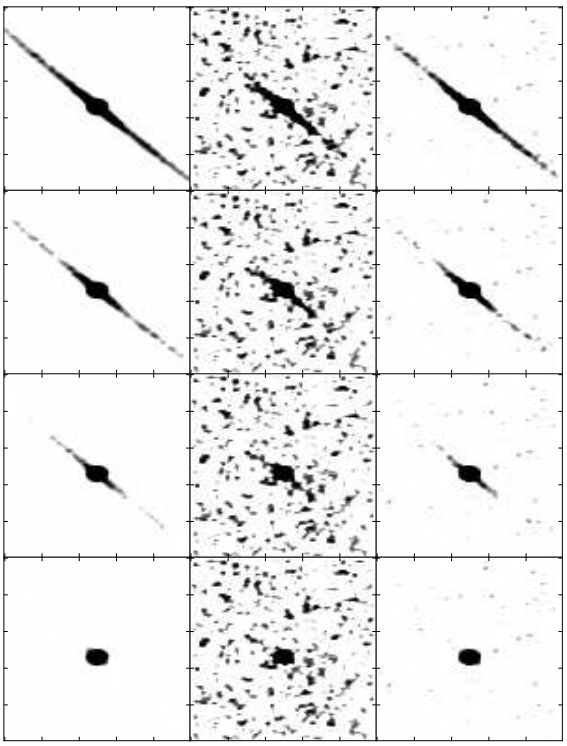

Figure 1. Output of the simulations. Each panel covers 6° by 4° on the sky. The left column shows the number of simulated cluster and tail stars. The central column shows the total number of simulated stars, cluster, tail and field, after subtraction of the average number over the entire simulation field (star counts method). The right column shows the output of the matched-filter, γ_{cl}, as described in §2.

3.2 Palomar 5

In order to further validate our algorithm we have chosen the halo globular cluster Palomar 5. This cluster has the most prominent tidal tail known to date, making it a good test case for any detection algorithm.

Our analysis was carried out using the Sloan Digital Sky Survey (SDSS) Data Release 7 (DR7) (Abazajian et al. 2009). SDSS is a large survey, covering up to 10000 square degrees of the northern and part of the southern galactic cap, using 5 filters ($ugriz$). Its large continuous area coverage and photometric homogeneity make it a very useful data set for the discovery of tidal tails or any other large scale sub-structure in the Galaxy.

Although SDSS reaches r magnitudes up to 23.5, we avoid stars fainter than 22.5. This conservative limit is set to avoid any complications due to miss-classification of stars and galaxies.

F_{cl} was built using a circular region around the center of Palomar 5 with a 0°.13 radius. Figure 3a shows the $r \times (g - r)$ Hess diagram constructed using the stars located inside this circular region. Some of the expected features of a typical GC are visible: a main-sequence (MS), MS turn-off (MSTO), Red Giant Branch (RGB), and Horizontal Branch (HB). The choice of contour levels of Figure 3 is such that the Asymptotic Giant Branch (AGB), and the Blue Stragglers (BS) are not visible despite being present in this cluster. To avoid minor contributions of background stars in the region where F_{cl} was built, we only used stars that occupy the loci expected for a GC population.

As discussed on previous sections, F_{bg} is expected to vary over large scales. To accommodate some of this variation, we follow the prescriptions of Rockosi et al. (2002) and take the average Hess diagram of four 3 deg^2 fields far away from Palomar 5. The fields used are centred in same coordinates as in Rockosi et al. (2002). The resulting Hess diagram is shown in Figure 3b. This approach to the construction of F_{bg} is such that the spatial dependency should be reduced, hence simplifying the solution of equation (7). We thus apply the MF under the assumption that the background term

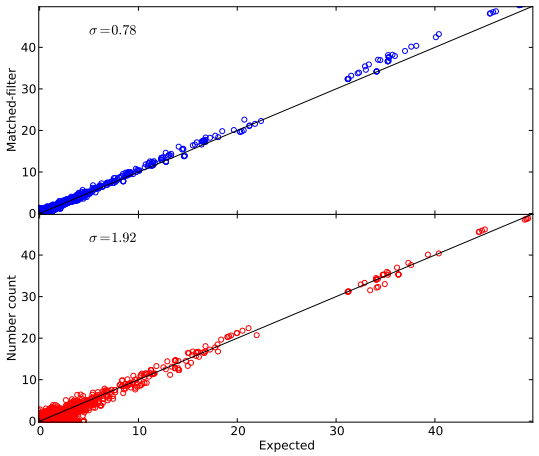

Figure 2. Comparison between the simulated number of cluster stars (in the x-axis) with the number derived from simple number counts (lower panel) and from the matched-filter (upper panel). The identity line is shown on both panels. The dispersion is also indicated on the top left corner of each panel.

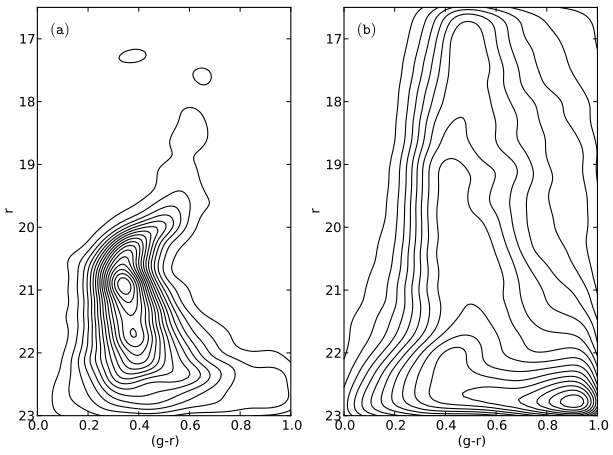

Figure 3. Panel *a*: $r, (g-r)$ F_{cl} contours on the CMD plane for the Palomar 5 SDSS data. Panel *b*: same as in panel *a* but now showing the F_{bg} contours. In both panels the contour levels are normalized to the range varying from 0 to 1, and are evenly spaced spaced by 1/20.

does not vary with position. The measured background is of 0.51 $arcmin^{-2}$. Figure 4 shows the smoothed (0.1 *deg* Gaussian smoothing) distribution of stars consistent with Palomar 5 stellar population.

Having F_{cl} and F_{bg} properly constructed, we may retrieve the best estimate of the density of stars consistent with F_{cl} in any region of the sky where F_{bg} well describes the Galaxy field star population. We applied the matched-filter to a region $226^\circ < RA < 231^\circ$ and $-1.1^\circ < Dec < 1.1^\circ$, which was divided in a grid of 0.03×0.03 *deg* bins. Figure 4 shows the results of the matched-filter as a stellar surface

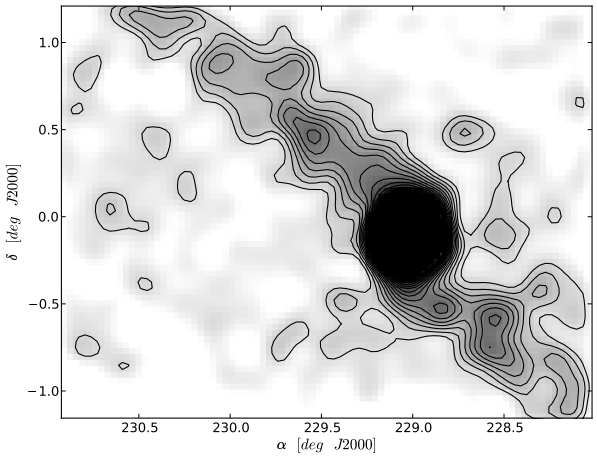

Figure 4. The stellar number density map resulting from the MF applied to SDSS data around Palomar 5. We show the number of stars in grey scale. The contour map emphasizes the more populated regions. The 4 outermost contours correspond to 0.1,0.15,0.20,0.25 star $arcmin^{-2}$. Near the centre of Palomar 5 we do not show any contour for clarity.

density of Palomar 5 like stars overlaid on a residual contribution by background stars (i.e. the last term on equation 7).

The extra-tidal structure recovered for Palomar 5 closely resembles the one found in previous works using the MF technique. The peak of density along the tail is expected to be of ~ 0.2 $arcmin^{-2}$ according to Odenkirchen et al. (2003). In this work we find a maximum density of ~ 0.27 $arcmin^{-2}$ using a different set of colours and magnitudes.

The recovered Palomar 5 tail extends throughout 1.8 *deg*, ending at the edge of the analysed field, which suggests a tail that extends much further, as depicted by Odenkirchen et al. (2003). Several density fluctuations are found along the tail. Most of these were also found on these previous studies. The fluctuations are expected even for the simplest of the orbits such as circular orbits on a axisymmetric potential (Küpper et al. 2010; Küpper, MacLeod, & Heggie 2008).

4 NGC 2298

NGC 2298 (also designated by ESO 366-SC 022) is located at $l = 245^\circ.63$, $b = -16^\circ.01$, therefore projected towards the Galactic anti-centre. Its position places it near the Galactic disk. It is thus superimposed on to the thin and thick disks, besides the halo. Structural parameters were found by De Marchi & Pulone (2007), such as core radius $r_c = 0'.29$ and tidal radius $r_t = 8'.0$ leading to a concentration parameter of $c = log(r_t/r_c) = 1.44$. The distance and metallicity taken from Harris (1996) are $d = 10.80\,kpc$ and $[Fe/H] = 1.85$. The analysis of the HST/ACS CMD from those authors also yielded an extinction of $E(B-V) = 0.15$ towards the cluster.

We here describe a first attempt to detect an extra-tidal structure around NGC 2298, using a field of $\simeq 4$ sq. deg around the cluster. Its location towards a dense stellar

field, with likely varying extinction, makes it a harsher test to the MF method that we implemented. NGC 2298 is one of the GCs located in the footprint of DES. Therefore, DES will provide a much larger area coverage around the cluster, making it possible to make follow-up studies using the same methods developed for this paper.

4.1 Data

NGC 2298 was observed using the MOSAIC2 camera located at the 4 meter Blanco Telescope at Cerro Tololo International Observatory (CTIO). The MOSAIC2 instrument is a $8192px \times 8192px$ segmented CCD camera with a Field of View (FOV) of $36' \times 36'$. Each of the 8 camera segments is a CCD with $4096px \times 2048px$. Separating each CCD there is a gap of 35 $px = 9.2''$ in the East-West direction and 50 $px = 13.2''$ in the North-South direction. The wide field of MOSAIC2 makes it the best instrument for large area observations in the southern hemisphere.

The observations took place in the night of February 10th 2010 under photometric conditions. The mean seeing for the night was 0.7", which is normal for the epoch . We observed 12 overlapping fields around NGC 2298 in two passbands, V and I. Figure 5 show the fields and their CCD segments overlaid on a Digital Sky Survey (DSS) image around the cluster. The fields in the Figure have been corrected for geometric distortions, as explained latter. The total exposure time was of 240 s (2×120 s) in the V band and 360 s ($3x120$ s) in the I band. The standard stars used for photometric calibration are taken from Stetson (2000). They are located within $30'$ of the cluster centre and were observed several times during the night, each time using one single short exposure in the V and I bands. MOSAIC2 was set to 1×1 binning on the 8-channel mode.

The reduction of the data was carried out using the `MSCRED` package running on the `IRAF` environment. All frames were reduced using standard procedures (crosstalk, overscan, bias, flatfield). Some complications arise when dealing with large field instruments. The FOV of MOSAIC2 introduces a spatial variation on the pixel size going from 0.27"/px in the centre of the FOV to 0.29"/px on the edges. This means that each exposure from a given field must be corrected for distortion before being stacked, since the projection depends on the pointing of the telescope. To correct for distortion each frame must have a reasonably accurate astrometric solution. This was done by constructing an initial guess for the World Coordinate System (WCS). This initial guess was determined using USNO-A catalogues [2]. With the initial guess for the WCS, we refine the astrometric solution frame by frame using the task `MSCCMATCH`. Frames that will be later combined are registered using `MSCIMATCH` and finally, using the task `MSCIMAGE`, all frames were corrected for distortions and combined into a single image. Since the process of distortion correction involves a re-sampling of the pixels, the bad pixel areas suffer distortions in the process due to the artificial step discontinuity in the image. To overcome this problem, the bad pixel masks were also corrected for distortions and later applied to the final combined image.

[2] Made available to the community at http://www.ctio.noao.edu/mosaic/

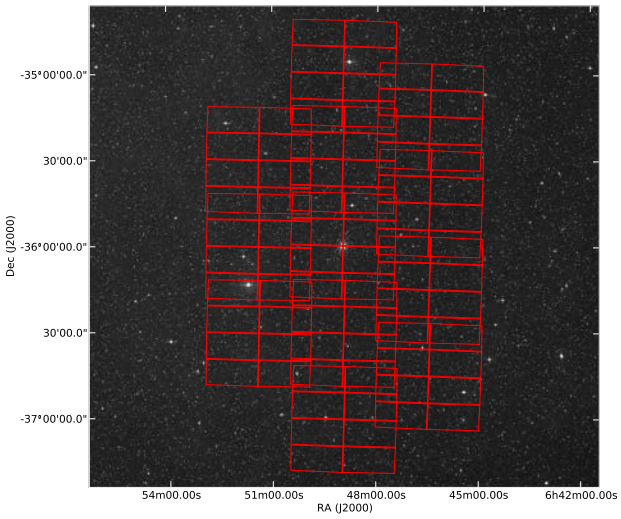

Figure 5. 3×3 *deg* DSS r band image with the borders of the 12 observed MOSAIC2 FOV overlaid in red. Notice the complex shapes introduced by the gaps between the CCDs.

4.2 Photometry

With the final combined images we performed point spread function (PSF) fit photometry using the broadly used `DAOPHOT` software Stetson (1994). All the photometry was performed by an automated python script. The script deals with each of the 8 MOSAIC2 chips independently since there may be PSF variations from one chip to another. The list below shows the steps taken to accomplish the photometry for each chip.

i. Find sources above 4 σ_{sky} (`DAOFIND`).
ii. Run aperture photometry (`PHOT`).
iii. Construct the PSF model using bright non-saturated and isolated stars.
iv. Fit the PSF model for each source (`ALLSTAR`).
v. Transform from physical to world coordinates.

In addition, the PSF was allowed to vary over each chip to account for any residual distortions. After this process, we combined the photometric tables from the two filters using a positional matching in world coordinates.

The combined VI photometric table for each field was calibrated using the following calibration equations:

$$\begin{aligned} V &= v + a(V-I) + bX + v_0 \\ I &= i + c(V-I) + dX + i_0 \end{aligned}$$

Where V (I) is the calibrated magnitude, v (i) is the instrumental magnitude, $(V-I)$ is the calibrated colour, X is the airmass, and v_0 (i_0) is the zero-point. The coefficients (a, b, c, d), as well as the zero-points, were obtained from a fit to the magnitudes and colours of the standard stars observed during the night with air-masses ranging from 1.01 to 2.60.

The final step to the data reduction is to apply aperture corrections. These corrections are necessary since there

may be *seeing* variations from field to field. The aperture corrections were determined using the overlapping regions on adjacent fields, starting by the central pointing, which contains the cluster and the standard stars.

To eliminate spurious detections, and possibly galaxies, we performed a cut in the magnitude error of the final photometric table. This cut eliminates sources with errors larger than those expected for point sources at their magnitude value. This process eliminates most spurious detections including many galaxies that could introduce uncertainties to the tidal tail detection.

The final photometric sample has approximately 152000 stars. The mean photometric error in the range $16 \leqslant V \leqslant 22$ is less than 0.05, which is enough for our purposes. All magnitudes were corrected for extinction using Schlegel, Finkbeiner, & Marc (1998) dust maps. The mean reddening for the entire observed region is $E(B-V) = 0.20$.

In Figure 6a we show the CMD for the stars within $12' =\sim 37\ pc$, which corresponds to 1.5 tidal radius as quoted by De Marchi & Pulone (2007). The structure of the CMD is typical of an old metal-poor GC. Note that at bright magnitudes we lose stars due to saturation, although the blue end of the extended HB is still visible. Larger errors on brighter magnitudes are due to saturation in the I band. In Figure 6b we show the CMD for stars outside $12'$, in this plot we choose to display only a fraction of 10% of the total number of points for clarity.

Using the best determination of NGC 2298 age and metallicity (De Marchi & Pulone 2007), we overlay the corresponding Padova isochrone to the data in Figure 6a. The best fit occurs for a distance modulus of $(m-M) = 15.15$, which closely agrees with the estimate from Harris (1996). However, a (V-I) offset of 0.06 towards blue colours was applied to properly fit the isochrone to the MS and MSTO. This offset reflects the discrepancy between the reddening value from the Schlegel, Finkbeiner, & Marc (1998) dust maps, $E(B-V) = 0.20$, and that found by De Marchi & Pulone (2007). In what follows, for the sake of coherence, we use the Schlegel, Finkbeiner, & Marc (1998) values over the entire field covered by our MOSAIC2 data.

For completeness reasons we chose not to match stars in overlapping regions. All the analysis was done on a field by field basis and, when necessary, we adopt the proper area correction (e.g. border of the fields and chips) using a carefully constructed mask. This mask also takes bad pixel regions into account when calculating any area. All areas calculated hereafter were obtained by a Monte-Carlo integral and accounting for the mask we built. See Balbinot et al. (2009) for further details.

4.3 Cluster structure

To make and independent measurement of NGC 2298 structural parameters we built its radial density profile (RDP). The RDP was built by counting stars in radial bins out to the point where the background is clearly reached. For the cluster center, we simply used values given in the literature.

In figure 7 we show the resulting RDP for NGC 2298. We choose not to use the cluster most central region due to incompleteness caused both by crowding and gaps on the CCD mosaic. Our RDP analysis covers out to an angular distance of $25'$ which corresponds to 78 *pc*. This is approximately three times the best estimated of tidal radius found in the literature. We fitted a King profile with fixed core radius ($r_c = 0.29 = 0.9pc$) since our central densities are not accurate due to crowding. We find a larger tidal radius of $r_t = 15'.91 \pm 1'.07$, which corresponds to 50 *pc*, which is twice larger than previously found. The background density found is of $\sigma_{bg} = 9.50 \pm 0.10\ stars/arcmin^2$.

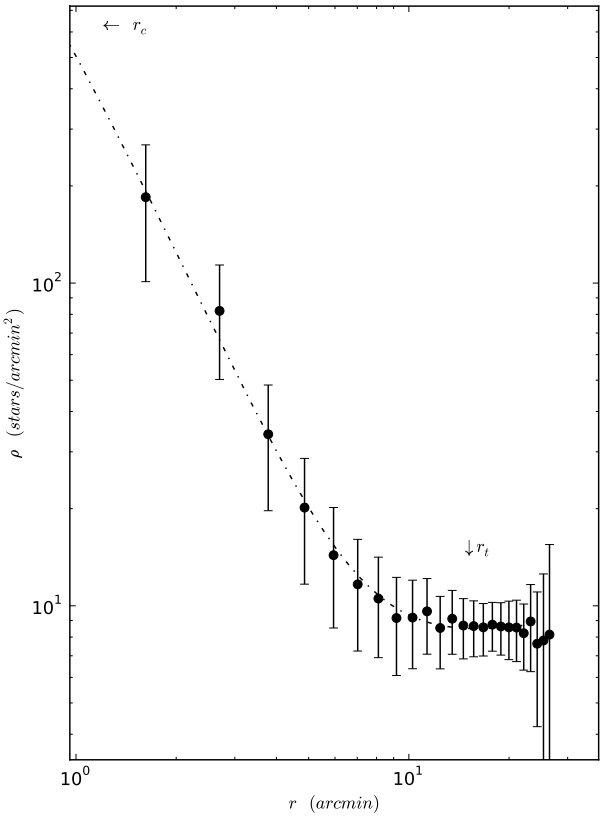

Figure 7. The logarithmic scale RDP for NGC 2298 with 1σ error bars. The dot-dashed line show the best fit of a King profile with a core radius fixed at $r_c = 0'.29 = 0.9pc$, as found in the high resolution data from De Marchi & Pulone (2007). The best fit values are $r_t = 15'.91 \pm 1'.07$ with a background density of $\sigma_{bg} = 9.50 \pm 0.10\ stars/arcmin^2$. The tidal and core radius positions are indicated. Notice that the core radius is out of bounds in this plot.

The last time NGC 2298 was observed with such a large FOV and photometric depth was by Trager et al. (1995). The authors find a tidal radius of $6'.48$ although not reaching deep magnitudes. Later, De Marchi & Pulone (2007) found a tidal radius of $8'.0$, although using only data that cover a $3.4 \times 3.4 arcmin$ FOV. Hence their estimated tidal radius relies on data that do not reach the full extension of the cluster. Our determination combines the advantages of larger depth compared to photographic plates and larger FOV compared to HST/ACS.

NGC 2298 was one of the first globular clusters to be found with a high degree of depletion of low mass stars (De Marchi & Pulone 2007). The inverted mass function and the low concentration parameter are expected for old globular

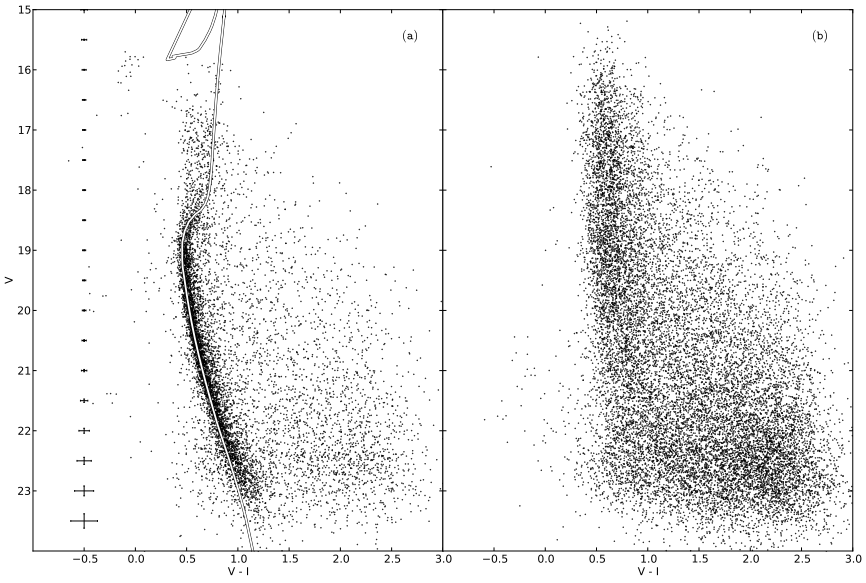

Figure 6. Panel *a*: $V,(V-I)$ CMD of NGC 2298 where only stars inside $r = 37pc$ where chosen. The mean photometric error is shown in the extreme left of this panel. We also show the best fit isochrone with $(m-M) = 15.15$ and the $(V-I)$ offset of 0.06 explained in the text. Panel *b*: $V,(V-I)$ CMD for stars outside $r = 37pc$. Only 10% of the total stars are shown for clarity.

clusters that are subject to a high degree of tidal interactions Baumgardt & Makino (2003).

Based on the fitted isochrone, the mass range sampled by our observation of NGC 2298 is very limited $0.6 \leqslant M_{\odot} \leqslant 0.79$. The inner parts of NGC 2298 are not accessible to us due to crowding. On the outer parts the number of stars is too low at our photometric depth, giving low statistical significance to the mass function. We thus refrain from making a PDMF reconstruction with our CTIO data; deeper observations covering a wider range of masses, such as those that will be provided by DES, are necessary to accurately determine the slope of the mass function in the outskirts of NGC 2298.

4.4 Extra tidal structure

We follow the same MF recipe adopted for Palomar 5 in §2 in order to investigate the presence of tidal tails associated NGC 2298. F_{cl} was built using stars that are less than 37 pc from NGC 2298 centre. As seen on figure 6, a relatively large amount of field stars are present on the region chosen to build F_{cl} . These field stars were eliminated by choosing a CMD locus that is consistent with the cluster evolutionary sequence in the same fashion as in Balbinot et al. (2009). F_{bg} was built using 6 fields near the edges of the observed region.

In figure 8 we show the resulting star count map for NGC 2298 after applying the MF. Several features are found above the 1σ confidence level. One interpretation of our findings is that the extended Northwest tail is the trailing tail since its orientation is opposed to the proper motion (Dinescu et al. 1999). The two smaller opposing structures found in the central East-West direction may be the result of tidal interaction with the disk, since they point towards the disk and NGC 2298 is close to the Galactic plane. In addition, a faint structure appears ahead of NGC 2298's motion, which may be the leading tail. The two structures found at the extreme North and South most likely are boundary effect introduced by the smoothing process. At last, a strong Northeast structure appears in the direction perpendicular to the Galactic disk. This may be interpreted as stars that have left the cluster although have not had time to fall behind or ahead of the orbit. Another faint structure opposite to the previous one is present, although not connected to any other enhancement.

Our findings are similar to those predicted by Combes, Leon, & Meylan (1999). The authors simulations predict a formation of multiple perpendicular tails in a cross-like pattern resulting from multiple disk crossings.

We do not discard the possibility that some of the features detected are in fact due to wrong extinction corrections. They could result from high frequency structures on the dust filaments close to the disk. These structures are not properly sampled due to resolution limitations of the Schlegel, Finkbeiner, & Marc (1998) maps built using IRAS that has a $FWHM = 6'.1$. However, most of the structures seen in figure 8 extend along many IRAS FWHMs and thus are likely to be real.

5 EFFECTS OF MASS SEGREGATION

So far, the MF technique has been applied without any assessment of the influence of improperly built F_{cl} . That is, if F_{cl} does not reflect the distribution of cluster stars in the colour-magnitude space, as well as its variations, throughout the entire FOV, the application of the MF may lead to miss identifications of tidal structures. One phenomenon that may give rise to an improper F_{cl} is mass segregation.

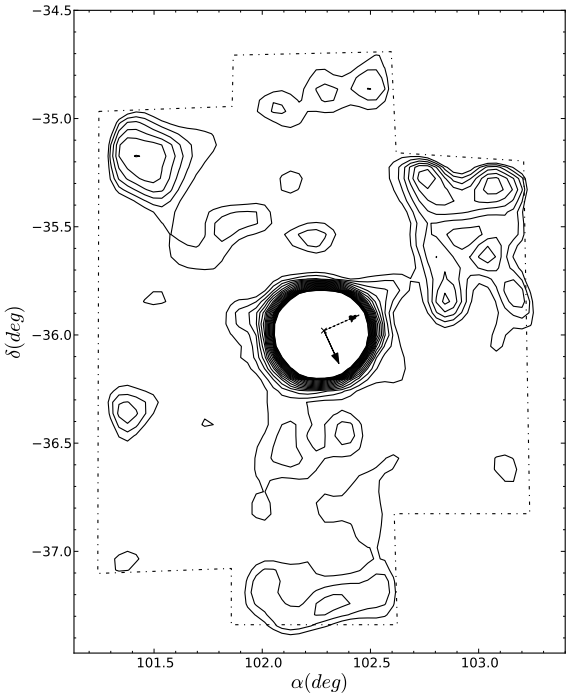

Figure 8. The result of applying the MF to NGC 2298 CTIO data. We show the derived number of stars, γ_{cl}, in a contour plot. The first three contour levels correspond to $0.8, 1.8, 2.8\sigma$ above background. The inner contours start at the tidal radius of the cluster. The dashed arrow points to the direction perpendicular to the Galaxy disk. The solid line points towards the proper motion direction (Dinescu et al. 1999). The resulting map was smoothed using a $0°.06$ Gaussian kernel, thus enhancing structures with a typical size similar to r_t.

Distance (pc)	α
0.5	1.6
1.5	1.1
2.5	0.5
3.5	0.1
4.5	0.0
5.5	−0.1
6.5	−0.5
7.5	−1.1
8.5	−1.6
$r \leqslant 9.5$	−1.6

Table 1. PDMF power law slopes for different annuli. Column 1 shows the distance range in *parsec*. Column 2 shows the simulation power law slopes for the mass range of $0.08 - 0.80\ M_{\odot}$.

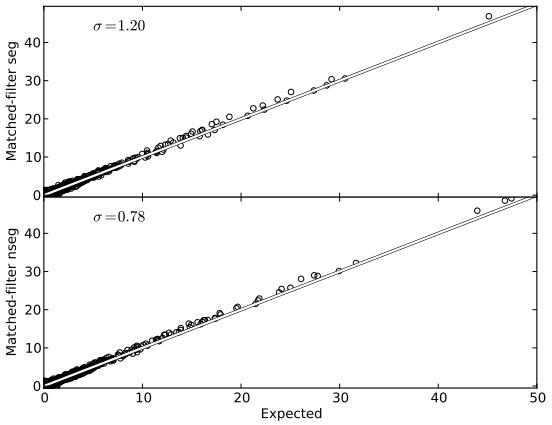

Figure 9. Comparison of the number of cluster stars detected using the MF (vertical axis) with the actual number of simulated stars (horizontal axis). The top panel shows the comparison for a mass-segregated cluster, whose PDMF slopes are listed in Table 1. The bottom panel shows the comparison for a non-segregated cluster. The identity line is shown on both panels. The dispersion in the plots are indicated at the top left.

We here attempt to quantify its effect on a model cluster consistent with NGC 2298.

To assess what is the effect of mass segregation on the MF technique, we made another simulation of a GC similar to NGC 2298, but now using the present day mass function (PDMF) from the literature. Since the slope of the PDMF is only determined to a distance of $1.8'$, we extrapolate it to $3.6'$ by assuming the same growth rate of the PDMF slope as in the inner parts of NGC 2298. For the outermost parts of the cluster, we assume that the PDMF slope saturates at the value at $3.6'$. This latter value, therefore, is the one that applies to most extra-tidal stars in the model. Table 1 lists the model slopes at different distances from cluster centre. We also run another simulation, which is identical to the previous one, but without mass segregation. In this second, non-segregated case, the PDMF slope used is the one corresponding to the outermost bin in Table 1.

The simulation parameters and number of simulated stars in these two extra simulations are the same as in §3.1, except for the PDMF slopes, as described. The background of stars is also the same one used in that section, built using `TriLegal`.

In figure 9 we show the comparison of the true number of cluster stars to those detected using the MF, in cases when mass-segregation is present and absent. Notice that there are no systematic changes in the number of stars obtained in either situation. However there is a significant difference on the dispersion, in that the MF reconstructed star counts have larger scatter in the cluster which is subject to mass segregation. We thus conclude that, even though the detection of a tidal tail is still possible in presence of mass segregation effects, the limiting distance out to which the tail may be detected, as well as some of its low-density substructure, may be affected if F_{cl} does not properly take segregation into account.

6 DISCUSSION

We developed an implementation of the MF technique that is relatively user-independent and with great potential for being used in large scale. These features make it suitable to be applied to deep and wide angle, such as DES, SDSS, PanSTARSS and LSST, in a systematic way to find GC tidal tails and other MW halo sub-structures.

The MF was tested on simulated data, showing that it increases the contrast of the tail relative to the background by a factor of 2.5 for a cluster projected against a dense background, similar to that of a low latitude GC, such as NGC 2298. The MF was also tested on a real scenario were it successfully recovered the tidal tail of Palomar 5. The Pal 5 tail closely resembles previous detections in the literature, reproducing both shape and density.

We then study the GC NGC 2298, which is a good candidate to have a tidal tail due to its previously studied PDMF and location. We found that the cluster has a tidal radius of $r_t = 15'.91 \pm 1'.07$ when a King profile is fitted and keeping the core radius fixed ($r_c = 0'.29$). Our r_t value is almost twice what was previously found in the literature. It is based on deeper photometry than previous photographic work and on a much wider area than previous high-resolution and deep photometry. The new value for r_t changes the concentration parameter of NGC 2298 to $c = 1.44$, pushing it further away from the $\alpha - c$ relation from De Marchi, Paresce, & Portegies Zwart (2010). This discrepancy makes us wonder if the tidal radius of other clusters like NGC 6838 and NGC 6218 are not similarly affected by observational biases associated to small fields or shallow photometry. For instance NGC 6218 has a tidal radius of $17.2'$ whereas observations only cover $3.4'$ (De Marchi, Pulone, & Paresce 2006). There are no publications available for NGC 6838 to properly access if its tidal radius determination uses data that extends beyond its literature tidal radius. We point out that the determination of the tidal radius of Palomar 14 by Sollima et al. (2011) also shows an increase by a factor of 4 when compared with to previous determinations in the literature. The increase of the tidal radius appears to be a trend in the sense that whenever large FOV are used the tidal radius increases.

Applying the MF technique to NGC2298, we find that this GC has several extra-tidal structures detected above 1σ confidence level. The strongest feature is the elongation of the cluster along the direction of the disk, suggesting strong tidal interaction. We also find what appears to be faint leading and trailing tails, both extending to the edges of the observed field ($\sim 1°.5$). At last a large structure is found, spreading from the cluster towards the disk direction. This structure may be a halo of NGC 2298 that got ejected on the last disk crossing.

Follow up observations are necessary to properly access the nature of each extra-tidal structure found around NGC 2298. We expect DES to give this follow up. The survey is going to reach 1 mag deeper than our observations with a much larger area, better photometric calibrations, and 3 more passbands. DES will thus allow us to analyze the extra-tidal structure of NGC 2298 in more detail and over larger distances. A larger area will also enable us to test sophistications to the SSP and background models underlying the MF, such as a varying background.

Finally, we simulate a cluster with and without mass segregation to evaluate how mass segregation affects the MF results, via an F_{cl} that does not adequately describe the CMD in the outer regions of a mass-segregated cluster. We find that there is no strong systematic effect in the reconstructed density of stars. There is, however, a significant difference in the density fluctuations relative to the truth table, in the sense that the the mass-segregated cluster has a larger dispersion around the simulated densities. This is the result of its F_{cl} not being able to accommodate the variation in the CMD caused by a position dependent PDMF. We thus conclude that the impact of unaccounted for mass segregation in the MF process is to make it more difficult to detect the full extension and the structural details of a GC tidal tail, rather than preventing the tidal tail detection per se. From our knowledge, this is the first time the MF was tested for an intrinsically variable and unaccounted for F_{cl} .

Acknowlegments.

We are grateful to the CTIO local staff for the help during observation/reduction. We acknowledge support from Conselho Nacional de Desenvolvimento Científico e Tecnológico (CNPq) in Brazil.

We also thank the support of the Laboratrio Interinstitucional de e-Astronomia (LIneA) operated jointly by the Centro Brasileiro de Pesquisas Fisicas (CBPF), the Laboratrio Nacional de Computao Cientfica (LNCC) and the Observatrio Nacional (ON) and funded by the Ministry of Science and Technology (MCT)

REFERENCES

Abazajian K. N., et al., 2009, ApJS, 182, 543
Andreuzzi G., De Marchi G., Ferraro F. R., Paresce F., Pulone L., Buonanno R., 2001, A&A, 372, 851
Balbinot E., Santiago B. X., Bica E., Bonatto C., 2009, MNRAS, 396, 1596
Baumgardt H., & Makino J., 2003, MNRAS, 340, 227
Binney J., & Tremaine S., 1987, Galactic Dynamics, (Princeton University Press)
Combes F., Leon S., Meylan G., 1999, A&A, 352, 149
De Marchi G., Paresce F., Portegies Zwart S., 2010, ApJ, 718, 105
De Marchi G., Pulone L., 2007, A&A, 467, 107
De Marchi G., Pulone L., Paresce F., 2006, A&A, 449, 161
DePoy D. L., et al., 2008, SPIE, 7014,
Dinescu D. I., van Altena W. F., Girard T. M., López C. E., 1999, AJ, 117, 277
Doyle L. R., et al., 2000, ApJ, 535, 338
Girardi L., Groenewegen M. A. T., Hatziminaoglou E., da Costa L., 2005, A&A, 436, 895
Girardi L., Bressan A., Bertelli G., & Chiosi C., 2000, A&AS, 141, 371
Grillmair C. J., Johnson R., 2006, ApJ, 639, L17
Leon S., Meylan G., Combes F., 2000, A&A, 359, 907
Harris W.E., 1996, AJ, 112, 1487
Johnston K. V., Sigurdsson S., Hernquist L., 1999, MNRAS, 302, 771
Kepner J., Fan X., Bahcall N., Gunn J., Lupton R., Xu G., 1999, ApJ, 517, 78
Kerber L., Santiago B., Castro, R. & Valls-Gabaud, D., A&A, 390, 121
King I. R., Hedemann E., Jr., Hodge S. M., White R. E., 1968, AJ, 73, 456
Koch A., Grebel E. K., Odenkirchen M., Martínez-Delgado D., Caldwell J. A. R., 2004, AJ, 128, 2274
Koposov S. E., Rix H.-W., Hogg D. W., 2010, ApJ, 712, 260

5 *Conclusões e perspectivas*

Nesta dissertação apresentamos três trabalhos realizados com a finalidade de averiguar os efeitos ambientais sobre a dinâmica de aglomerados de estrelas dentro do Grupo Local. Os estudos foram baseados em técnicas de análise do CMD das estrelas individuais de cada aglomerado.

Baseados na fotometria de alta precisão e resolução espacial do aglomerado NGC 6642 concluímos que este aglomerado possui um núcleo colapsado. Sua função de massa apresenta uma forma invertida no domínio de massas analisado ($0,4 \leq M(M_{\odot}) \leq 0,8$), possuindo mais estrelas de alta massa do que de baixa massa. Também encontramos indícios que a população de *blue stragglers* está localizada nas regiões mais centrais, quando comparadas com estrelas de massa similar, favorecendo assim o cenário de que estas estrelas foram formadas a partir da fusão de outras estrelas. Por fim, encontramos que NGC 6642 possui uma idade de $13,8 \pm 1,6$ Gyr e uma metalicidade $[Fe/H] = -1,80 \pm 0,20$. Este aglomerado está localizado a 8 kpc do Sol e a apenas $1,4$ kpc do centro da Galáxia. O colapso do núcleo de NGC 6642 pode ser facilmente entendido tendo em vista a sua grande idade, o que possibilitou que suas estrelas atingissem este estágio dinâmico. O fato de NGC 6642 possuir uma função de massa invertida é entendido no contexto de choques com o bojo e interação forte de maré, efeitos que sabidamente tem a capacidade de alterar sensivelmente a forma da função de massa.

Utilizando dados do imageador óptico SOI instalado no telescópio SOAR analisamos 3 candidatos à lacuna de idades da LMC. Uma técnica de descontaminação de estrelas de campo foi desenvolvida e testada em experimentos controlados, provando-se eficaz. Esta técnica foi utilizada para descontaminar os campos dos 3 aglomerados observados na LMC. Ao longo da análise dos dados constatou-se que um dos aglomerados candidatos não fora observado corretamente, restando apenas 2 candidatos à lacuna de idades em nossa amostra. O ajuste de modelos de evolução estelar para estes candidatos à lacuna de idades, provou que estes objetos não possuem idades consistentes com a lacuna. A massa dos aglomerados estudados é pequena quando comparada a aglomerados típicos da LMC. No entanto, nenhum deles pertence a lacuna de idades, o que nos leva a pensar que os aglomerados formados entre $4-10$ Gyr são

ainda menos massivos. Já que existe uma população de estrelas de campo formada durante a lacuna de idades, devemos observar uma população de aglomerados associada a esta época de formação estelar. O fato de que nem mesmo os aglomerados menos massivos analisados aqui pertencem à lacuna de idades indica que possivelmente os remanescentes devem possuir massas ainda menores.

O tempo de dissolução para um aglomerado de $10^4 M_\odot$ é de ~ 8 Gyr na LMC (de Grijs et al., 2006). Hunter et al. (2003) encontrou uma idade de cerca de 6 Gyr, portanto esperava-se que os candidatos à lacuna de idades tivessem 75% de seu tempo de vida total. Porém, mostrou-se que nenhum dos candidatos analisados tem mais de 2 Gyr, equivalente a 25% do tempo de dissolução associado.

Por fim, o aglomerado NGC 2298 é estudado utilizando o imageador óptico MOSAIC2 de grande campo de visão. Uma região de ~ 3 $graus^2$ foi observada até magnitudes $V \sim 23$, com intuito de buscar estruturas além do raio de maré deste aglomerado. Com base no perfil radial de densidade, mostrou-se que NGC 2298 possui um raio de maré duas vezes maior que o da literatura, seguindo uma tendência para esse tipo de estudo, no sentido que maiores e mais profundos campos observados levam a maiores determinações do raio de maré. Neste estudo também foi desenvolvida e testada, em casos reais e simulados, uma implementação da técnica de *matched-filter* para detectar populações estelares esparsas. Esta técnica foi então aplicada a NGC 2298, revelando diversas estruturas além do seu raio de maré. Um estudo dinâmico mais detalhado e um campo maior são necessários para melhor caracterizar as estruturas encontradas. Contudo, a orientação destas estruturas é consistente com uma cauda de maré adiantada e atrasada em relação à órbita de NGC 2298.

A técnica de descontaminação de estrelas de campo, desenvolvida para análise dos aglomerados candidatos à lacuna de idades das LMC, será aplicada para aglomerados na ponte que liga a LMC com a SMC. Neste projeto buscamos determinar idades de aglomerados sobre a ponte e averiguar se estes objetos se formaram no local ou foram ejetados no último encontro entre a SMC e a LMC.

As ferramentas desenvolvidas nessa dissertação tiveram como motivação a subsequente aplicação em grandes *surveys* fotométricos como o *Dark Energy Survey* (DES), *Sloan Digital Sky Survey* (SDSS) e o *Large Synoptic Survey Telescope* (LSST). Em especial, uma variação da técnica de *matched-filter* está sendo aplicada ao novo *data release* (DR8) do SDSS para buscar galáxias satélites à Via Láctea. Posteriormente esta mesma técnica será aplicada aos dados do DES no hemisfério Sul, criando assim uma amostra homogênea da família de satélites da Via Láctea.

Grandes *surveys* fornecem fotometria de alta precisão em grandes ângulos sólidos. Estas características observacionais criam condições ideais para detecção de caudas de maré em aglomerados de estrelas, estendendo o número de ajuste de órbitas, impondo vínculos mais fortes sobre o potencial gravitacional da Galáxia. Além de determinar órbitas de aglomerados globulares, serão descobertas novas caudas de maré de galáxias acretadas no passado. Estas caudas também poderão ser usadas para modelar o potencial da Galáxia e impor vínculos sobre seu histórico de acresção.

Na astronomia atual muitas lacunas estão por ser preenchidas. Tomamos como exemplo a cosmologia, que fez e ainda faz previsões precisas sobre a formação de estruturas em larga escala. No entanto, sofre de problemas fundamentais, como inconsistências quanto à previsão do número de galáxias satélites da Via Láctea - um observável aparentemente simples. O processo de formação e evolução de galáxias acontece em escala muito menor que 1 Mpc, porém, a maior dificuldade de criar um modelo consistente para formação das galáxias reside na falta de conhecimento sobre o Grupo Local, em particular na falta de informação sobre a estrutura e distribuição das galáxias anãs satélites (Kroupa et al., 2010). Nesse sentido, a tendência para os próximos *surveys* será criar uma nova perspectiva não só sobre as pequenas escalas, mas sobre o Universo como um todo, tanto do ponto de vista da cosmologia tradicional quanto da cosmologia de campo próximo.

REFERÊNCIAS

Aguilar L., Hut P., Ostriker J. P., 1988, *On the evolution of globular cluster systems. I - Present characteristics and rate of destruction in our Galaxy*, ApJ, 335, 720

Andreuzzi G., De Marchi G., Ferraro F. R., Paresce F., Pulone L., Buonanno R., 2001, *VLT observations of the peculiar globular cluster NGC 6712. II. luminosity and mass functions*, A&A, 372, 851

Balbinot E., Santiago B. X., Bica E., Bonatto C., 2009, *The globular cluster NGC 6642: evidence for a depleted mass function in a very old cluster*, MNRAS, 396, 1596

Baumgardt H., Makino J., 2003, *Dynamical evolution of star clusters in tidal fields*, MNRAS, 340, 227

Bica E., Bonatto C., Blumberg R., 2006, *Faint open clusters with 2MASS: BH 63, Lyngå 2, Lyngå 12 and King 20*, A&A, 460, 83

Binney J., & Tremaine S., 1987, Galactic Dynamics, (Princeton University Press)

Boutloukos S. G., Lamers H. J. G. L. M., 2003, *Star cluster formation and disruption timescales - I. An empirical determination of the disruption time of star clusters in four galaxies*, MNRAS, 338, 717

Brodie, J. P., Larsen, S. S. (2002) *New members of the cluster family in nearby lenticular galaxies.* AJ, 124, 1410

de Grijs R., Anders P., 2006, *How well do we know the age and mass distributions of the star cluster system in the Large Magellanic Cloud?*, MNRAS, 366, 295

de Marchi G., Pulone L., 2007, *NGC 2298: a globular cluster on its way to disruption*, A&A, 467, 107

De Marchi G., Paresce F., Pulone L., 2007, *Why haven't loose globular clusters collapsed yet?*, ApJ, 656, L65

Forbes D. A., Lasky P., Graham A. W., Spitler L., 2008, *Uniting old stellar systems: from globular clusters to giant ellipticals*, MNRAS, 389, 1924

Geha M., Guhathakurta P., van der Marel R. P., 2003, *Internal dynamics, structure, and formation of dwarf elliptical galaxies. II. Rotating versus nonrotating dwarfs*, AJ, 126, 1794

Gilmore G., Wilkinson M. I., Wyse R. F. G., Kleyna J. T., Koch A., Evans N. W., Grebel E. K., 2007, *The observed properties of dark matter on small spatial scales*, ApJ, 663, 948

Harris W. E., 1996, *A catalog of parameters for globular clusters in the milky way*, AJ, 112, 1487

Koposov S. E., Rix H.-W., Hogg D. W., 2010, *Constraining the milky way potential with a six-dimensional phase-space map of the GD-1 stellar stream*, ApJ, 712, 260

Kroupa P., Famaey B., de Boer K. S., et al., 2010, *Local-Group tests of dark-matter concordance cosmology . Towards a new paradigm for structure formation*, A&A, 523, A32

Girardi, L., Bertelli, G., Bressan, A., Chiosi, C., Groenewegen, M. A. T., Marigo, P., Salasnich, B., Weiss, A. (2002) *Theoretical isochrones in several photometric systems. I. Johnson-Cousins-Glass, HST/WFPC2, HST/NICMOS, Washington, and ESO Imaging Survey filter sets.* A&AS, 391, 195

Girardi L., Bica E., 1993, *Colour evolution models and the distribution of Large Magellanic Cloud clusters in the integrated UBV plane*, A&A, 274, 279

Grillmair C. J., Johnson R., 2006, *The detection of a* 45deg *tidal stream associated with the globular cluster NGC 5466*, ApJ, 639, L17

Hunter, D. A., Elmegreen, B. G., Dupuy, T. J., Mortonson, M. (2003) *Cluster mass functions in the Large and Small Magellanic Clouds: fading and size-of-sample effects.* AJ, 126, 1836

Javiel S. C., Santiago B. X., Kerber L. O., 2005, *Constraints on the star formation history of the Large Magellanic Cloud*, A&A, 431, 73

Jensen J., Mould J., Reid N., 1988, *The continuity of cluster formation in the Large Magellanic Cloud*, ApJS, 67, 77

King I. R. (1992) *The structure of star clusters. I. an empirical density law.* AJ, 67, 471

Koposov, S., Belokurov, V., Evans, N. W., Hewett, P. C., Irwin, M. J., Gilmore, G., Zucker, D. B., Rix, H.-W., Fellhauer, M., Bell, E. F., Glushkova, E. V. (2008) *The luminosity function of the Milky Way satellites.* ApJ, 686, 279

Lada C. J., Lada E. A., 2003, *Embedded clusters in molecular clouds*, ARA&A, 41, 57

Larsen S. S., Brodie J. P., 2000, *Hubble Space Telescope observations of star clusters in NGC 1023: evidence for three cluster populations?*, AJ, 120, 2938

Mackey, A. D., Wilkinson, M. I., Davies, M. B., Gilmore, G. F. (2008) *Black holes and core expansion in massive star clusters.* MNRAS, 386, 65

Niederste-Ostholt M., Belokurov V., Evans N. W., Koposov S., Gieles M., Irwin M. J., 2010, *The tidal tails of the ultrafaint globular cluster Palomar 1*, MNRAS, 408, L66

Noël N. E. D., Gallart C., Costa E., Méndez R. A., 2007, *Old main-sequence turnoff photometry in the Small Magellanic Cloud. I. Constraints on the star formation history in different fields*, AJ, 133, 2037

Parmentier G., de Grijs R., 2008, *The poorly constrained cluster disruption time-scale in the Large Magellanic Cloud*, MNRAS, 383, 1103

Peng, E. W., Côté, P., Jordán, A., Blakeslee, J. P.; Ferrarese, L., Mei, S., West, M. J., Merritt, D., Milosavljević, M., Tonry, John L. (2006) *The ACS Virgo Cluster survey. XI. The nature of diffuse star clusters in early-type galaxies.* ApJ, 639, 838

Salaris M., Weiss A., Percival S. M., 2004, *The age of the oldest open clusters*, A&A, 414, 163

Spitzer L., Jr., Thuan T. X., 1972, *Random gravitational encounters and the evolution of spherical systems. IV Isolated systems of identical stars*, ApJ, 175, 31

Sollima A., Martínez-Delgado D., Valls-Gabaud D., Peñarrubia J., 2011, *Discovery of tidal tails around the distant globular cluster Palomar 14*, ApJ, 726, 47

Origlia L., Valenti E., Rich R. M., 2005, *High-resolution infrared spectra of NGC 6342 and 6528: two moderately reddened bulge globular clusters*, MNRAS, 356, 1276

Trager S.C., King Ivan. R., Djorgovski S. (1995) *Catalogue of galactic globular-cluster surface-brightness profiles.* AJ, 109, 218

Wilkinson, M. I., Hurley, J. R., Mackey, A. D., Gilmore, G. F., Tout, C. A. (2003) *Core radius evolution of star clusters.* MNRAS, 343, 1025